Engineering Fracture Mechanics 240 (2020) 107326

Contents lists available at ScienceDirect

Engineering Fracture Mechanics

journal homepage: www.elsevier.com/locate/engfracmech

# Evaluation of CTOD resistance curves in clamped SE(T) specimens with weld centerline cracks

Seyed Hamidreza Afzalimir, Vitor Scarabeli Barbosa, Claudio Ruggieri *

*Department of Naval Architecture and Ocean Engineering, University of São Paulo, São Paulo, Brazil*

ARTICLE INFO

*Keywords:*
CTOD
*J*-integral
Crack growth
CTOD-resistance curve
Clamped SE(T) specimen
Fracture assessments

ABSTRACT

This work addresses the characterization of the crack tip opening displacement (CTOD or $\delta$) for extending cracks in clamped single edge notched tension, SE(T), fracture specimens based upon fracture toughness tests and numerical analyses of stable crack growth conducted on specimen geometries extracted from pipe girth welds with different material properties. The study covers fracture resistance tests and crack growth analysis of plane strain and 3-D models for clamped SE(T) specimens with a weld centerline crack, in which a computational cell methodology to model Mode I crack extension in ductile materials is utilized to describe the evolution of $J$ and CTOD with increased loading for the extending crack. Laboratory testing of girth welds made of different materials provides the measured crack growth resistance curves from which the key microstructural parameters utilized in the growth analysis are calibrated. The present investigation shows that CTOD resistance curves based on the double clip-gage (DCG) procedure are consistently higher than the corresponding fracture resistance data based on $J-$CTOD relationships, thereby potentially yielding nonconservative fracture toughness estimates.

## 1. Introduction

Substantial progress has been made in recent years in developing and testing nonstandard specimen geometries to measure fracture toughness data, including tearing resistance properties, more applicable to defect assessments and fitness-for-service (FFS) analyses of structural components with crack-like flaws under low constraint conditions. A primary motivation to these activities emerged from the understanding of the potential strong dependency of fracture toughness on crack geometry, loading type and material strain hardening behavior. Crack-like defects in engineering components are very often surface cracks, predominantly loaded in tension, that form during fabrication (such as weld cracks and lack of fusion) or during in-service operation (commonly in the form of fatigue cracks at weld seams or environmental cracks). These cracked components develop low levels of crack tip constraint and stress triaxiality which are not well characterized by fracture testing of standard, deep notch specimens under high constraint conditions and loaded predominantly in bending. Indeed, the rather strong differences in constraint conditions between common structural defects and standard fracture specimens, including specifically the compact tension geometry, C(T), and the single-edge notch specimen under three-point (3P) bending, SE(B), having deep cracks ($a/W \geq 0.45$–$0.5$), provide a main obstacle in extending correlative fracture mechanics as a more effective engineering tool for defect assessment procedures.

A case of considerable relevance in connection with the previous arguments lies in the incorporation of the effects of ductile tearing

* Corresponding author.
*E-mail address:* claudio.ruggieri@usp.br (C. Ruggieri).

https://doi.org/10.1016/j.engfracmech.2020.107326
Received 13 July 2020; Received in revised form 18 September 2020; Accepted 19 September 2020
Available online 2 October 2020

in flaw acceptance criteria based on Engineering Critical Assessment (ECA) methodologies as structural steels commonly exhibit large increases in fracture toughness, as characterized by the $J$-integral [1,2], with stable crack extension of a crack-like flaw. Experimental studies to address constraint effects on the upper-shelf fracture toughness of ferritic steels (see illustrative examples in [3,4]) reveal a marked influence of specimen geometry, relative crack size, as characterized by the $a/W$-ratio, and loading mode (bending *vs.* tension) on crack growth resistance ($J-\Delta a$ or, equivalently, CTOD $-\Delta a$) curves (also termed $R$-curves). Here, the $J$-integral and the crack tip opening displacement (CTOD or $\delta$) describe the intensity of near-tip deformation [2,5] and $\Delta a$ is the amount of crack growth. For the same material, deeply-cracked C(T) and 3P SE(B) specimens provide lower $R$-curves while shallow-notch SE(B) geometries and single-edge notch tension, SE(T), specimens yield larger toughness values at similar amounts of ductile tearing, $\Delta a$.

Limiting specific attention to laboratory testing of fracture specimens to characterize ductile fracture behavior under low constraint conditions, much current research now focuses on standardization efforts for fracture testing of single edge notched tension, SE(T), specimens (also often termed SENT configurations) to measure experimental $R$-curves more applicable to girth welds of oil and gas transmission pipelines and marine steel risers. Early work to develop a testing protocol for this specimen configuration centered on the evaluation of crack growth resistance curves in terms of $J-\Delta a$ data [3,6,7] based on the unloading compliance (UC) method [8,9]. These studies were followed by more recent efforts addressing improved procedures to evaluate $J$ and $\Delta a$ based on extensive finite element analyses of SE(T) specimens with varying geometries and material properties, including different mismatch conditions for weld centerline notched specimens [4,10–14]. However, because of the widespread use of the CTOD parameter since its introduction in the 70s, when early development conducted at the Welding Institute introduced the concept of a CTOD design curve [15,16], current defect assessment procedures adopted by the oil and gas industry favor the utilization of CTOD $-R$ curves rather than $J$-resistance measurements. Here, existing testing methodologies under development to measure crack growth resistance properties for pipeline steels often adopt a double clip gage (DCG) procedure to estimate the crack tip opening displacement (CTOD) from experimental measurements of crack opening displacements (COD) at two different points in SE(T) specimens [17–20]. While used effectively in conventional fracture testing programs, the DCG procedure does not address explicitly the effects of stable crack growth on the relationship between remotely applied loading and crack-tip driving forces, here characterized in terms of the CTOD. Moreover, the CTOD derived from the DCG procedure is defined as the crack opening at the position of the original crack tip such that, with crack tip blunting and subsequent crack extension with increased remote loading, the position of the original crack tip falls behind the current crack tip. This features questions the proper measurement of the actual CTOD for a growing crack as well as the definition of meaningful CTOD values for use in defect assessment procedures.

This work addresses the characterization of the CTOD for extending cracks in clamped SE(T) fracture specimens based upon fracture toughness tests and numerical analyses of stable crack growth conducted on specimen geometries extracted from pipe girth welds with different material properties. The study covers fracture resistance tests and crack growth analysis of plane strain and 3-D models for clamped SE(T) specimens with a weld centerline crack, in which a computational cell methodology to model Mode I crack extension in ductile materials is utilized to describe the evolution of $J$ and CTOD with increased loading for the extending crack. Laboratory testing of girth welds made of different materials provides the measured crack growth resistance curves from which the key microstructural parameters utilized in the growth analysis are calibrated: (1) API 5L X80 pipeline steel; (2) ASTM A106 Gr C steel and (3) a typical C-Mn pipe internally clad with a nickel–chromium corrosion resistant alloy (ASTM UNS N06625 Alloy 625). Finite element analyses of a 3-D V-groove weld model for the UNS N06625 girth weld are also performed to assess 3-D effects on CTOD resistance curves derived from the DCG method and $J-$CTOD relationships. The numerical computations show relatively strong similarities between the $J$-CTOD relationships for stationary and growth analysis with important implications for experimental measurements of CTOD-resistance curves. Moreover, the present investigation shows that CTOD resistance curves based on the DCG procedure are consistently higher than the corresponding fracture resistance data based on $J-$CTOD relationships, thereby potentially yielding nonconservative fracture toughness estimates. The study provides a body of results which enables establishing more meaningful values of CTOD for use in ECA procedures incorporating SE(T) testing protocols for fracture toughness measurements.

## 2. Current evaluation procedures for $J$ and CTOD resistance data

Before launching into the characterization of the CTOD for growing cracks and the effects of different methods to determine CTOD resistance curves, this section presents key aspects of current evaluation procedures for $J$ and CTOD data which have a bearing on the present analyses. Implementation of the methodology essentially follows a conventional incremental procedure based on the unloading compliance (UC) technique using a single specimen test to determine the instantaneous value of $J$ and CTOD at periodic unloading steps during the measurement of the load *vs.* displacement curve thereby also enabling estimation of the amount of stable crack growth, $\Delta a$, at several locations on the load–displacement records. The presentation only focuses on salient features of estimation procedures for fracture toughness ($J$ and CTOD). Readers are referred to the articles of Zhu and Joyce [21], Zhu [14], Ruggieri [13] and references therein for details. The presentation begins by first considering an incremental procedure for evaluation of the $J$-integral based on experimental measurements of load and displacement records and then takes up two widely used approaches to determine the CTOD for extending cracks.

### 2.1. Incremental approach for experimental evaluation of the J-integral

A convenient approach (which forms the basis of current standards such as ASTM E1820 [22]) to evaluate $J$ with crack extension relies on the unloading compliance (UC) method [8,9] to update the elastic component, $J_e$, and plastic component, $J_p$, at each partial

unloading point, denoted $k$, during the test in the form

$$J_k = J_{e,k} + J_{p,k} \tag{1}$$

where the current elastic term is

$$J_{e,k} = \left(\frac{K_I^2}{E'}\right)_k, \tag{2}$$

and the current plastic term is given by

$$J_{p,k} = \left[J_{p,k-1} + \frac{\eta_{J-CMOD}^{k-1}}{b_{k-1}B_N}\left(A_{p,k} - A_{p,k-1}\right)\right] \cdot \Gamma_k \tag{3}$$

in which $\Gamma_k$ is defined as

$$\Gamma_k = \left[1 - \frac{\gamma_{LLD}^{k-1}}{b_{k-1}}\left(a_k - a_{k-1}\right)\right] \tag{4}$$

with factor $\gamma_{LLD}$ given by

$$\gamma_{LLD}^{k-1} = \left[-1 + \eta_{J-LLD}^{k-1} - \left(\frac{b_{k-1}}{W\eta_{J-LLD}^{k-1}}\frac{d\eta_{J-LLD}^{k-1}}{d(a/W)}\right)\right]. \tag{5}$$

In the above, $K_I$ is the elastic stress intensity factor for the cracked configuration, $E' = E/(1-\nu^2)$ where $E$ and $\nu$ are the (longitudinal) elastic modulus and Poisson's ratio, $A_p$ defines the plastic area under the load–displacement curve, $B_N$ denotes the net specimen thickness at the side groove roots, $b$ is the uncracked ligament ($b = W - a$ where $W$ is the width of the cracked configuration and $a$ is the crack length) and factors $\eta_{J-CMOD}$ and $\eta_{J-LLD}$ represent a nondimensional parameter which relates the plastic contribution to the strain energy for the cracked body and $J$. The incremental expressions for $J_p$ defined by Eqs. (3)–(5) contain two contributions: one is from the plastic work in terms of crack mouth opening displacement (CMOD) records and, hence, $\eta_{J-CMOD}$ and the other is due to crack growth correction in terms of LLD by means of $\eta_{J-LLD}$ (see Cravero and Ruggieri [23]).

The incremental methodology to evaluate the $J$-integral based on a single specimen has now become a standard procedure for fracture resistance testing of ductile materials, including the onset of stable crack growth and crack growth resistance curves. Moreover, as further shown in recent research and on-going work [13,24,25], the procedure is highly effective to characterize ductile tearing properties of pipeline girth weld materials which serve as a basis for ductile tearing assessments in ECA procedures applicable to oil and gas transmission pipelines and marine steel risers. Sections 5.2.2 and 5.2.3 address the evaluation of CTOD resistance curves directly from experimentally measured $J$-values based on the above incremental approach.

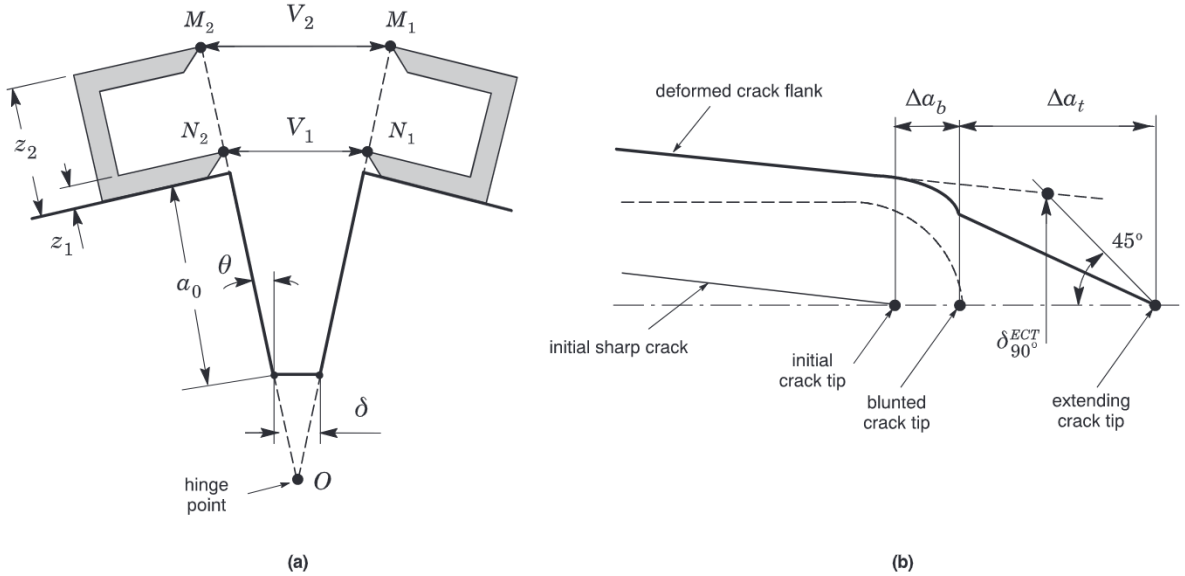


**Fig. 1.** (a) Double clip-gage (DCG) configuration to estimate the CTOD using measurements of crack opening displacements (COD) at two different points. (b) Evaluation of CTOD for an extending crack in which $\delta_{90^\circ}^{OCT}$ and $\delta_{90^\circ}^{ECT}$ denote the CTOD value based on the original crack tip and the extending crack tip.

### 2.2. CTOD evaluation procedure for extending cracks

A convenient approach to evaluate the crack tip opening displacement is based on the well established relationship between $J$ and CTOD ($\delta$) [26] and, thus, essentially relies on the $J$-integral evaluation procedure just outlined. The methodology determines the CTOD value from first evaluating the $J$-integral using the plastic work defined by the area under the load vs. CMOD curve and then the corresponding value of the CTOD using appropriate $J$ –CTOD relationships. The procedure simplifies evaluation of $\delta$-values using the same test protocol for $J$ while, at the same time, making use of the energy release rate definition of the $J$-integral. Existing test standards for $J$ and CTOD, including ASTM E1820 [22] and ISO 15653 [27] in the case of shallow notched bend specimens, adopt this method to evaluate the CTOD from experimentally measured records of load vs. displacements.

This framework also applies when the CTOD is employed to characterize the crack-tip driving force for a growing crack. To the extent that $J$ describes the crack-tip conditions with increased crack extension and, further, that a unique $J$ –CTOD relationship holds true for growing cracks, the CTOD at each partial unloading point, denoted $\delta_k$, during the test for an extending crack can be defined in terms of $J$ as

$$\delta_k = \frac{J_k}{m\sigma_f} \tag{6}$$

where $m$ represents a proportionality coefficient strongly dependent on the material strain hardening, but weakly sensitive to crack size as characterized by the $a/W$-ratio, and $\sigma_f$ represents the flow stress defined by $\sigma_f = (\sigma_{uts} + \sigma_{ys})/2$ in which $\sigma_{ys}$ and $\sigma_{uts}$ denote the yield stress and the tensile strength. In the above, the CTOD is most often evaluated by the 90° intercept procedure for numerical convenience in finite element analysis [5].

An alternative approach involves the use of a double clip-gage (DCG) arrangement to estimate the CTOD from experimental measurements of crack opening displacements (COD) at two different points. Fig. 1(a) schematically illustrates the procedure. By measuring two COD-values, $V_1$ and $V_2$, at two locations on a straight line passing through the crack flank of the specimen and assuming rigid body rotation, a geometrical relationship between the CTOD ($\delta$) and the measured COD-values is obtained in the form

$$\delta = V_1 - \frac{z_1 + a_0}{z_2 - z_1}(V_2 - V_1) \tag{7}$$

where $z_1$ and $z_2$ represent the distance of the measuring points for $V_1$ and $V_2$ from the specimen surface. Here, we note that the crack size, $a_0$, entering into Eq. (7) represents the initial crack length not the current crack size measured at the extending tip.

The above DCG approach is essentially applicable to a stationary crack since the CTOD is now defined as the crack opening at the position of the original crack tip, such that, with blunting and subsequent extension of the crack, the position of the original crack tip falls behind the current crack tip. By contrast, the extending crack-tip for a growing crack develops a sharp opening profile at the length-scale characteristic of the CTOD at onset of tearing as shown in Fig. 1(b). After a transitional behavior corresponding to the initiation of stable crack growth, crack extension arguably takes place under a nearly constant crack-tip opening angle (CTOA) which also implies a linear resistance curve for which the tearing modulus is constant. Sarzosa et al. [28] discuss this issue in detail with important potential implications for experimental measurements of CTOD-resistance curves. While a number of experimental studies support the assumption of a nearly constant CTOA value (or, equivalently, a constant $d\delta/da$ value) during stable crack growth, the tearing modulus is usually not constant during crack growth in many structural material, including typical pipeline steels. These arguments underline the difficulty (and perhaps some ambiguity) in adopting a proper and meaningful definition for the CTOD in the case of a growing crack.

However, since the primary interest here lies in addressing an evaluation procedure for the CTOD to characterize crack growth resistance properties applicable in ECA methodologies, we can advantageously adopt a procedure in which the intercept between a straight line at 45° from the *current* crack tip and the deformed crack flanks now defines the current value of CTOD for an extending crack, here denoted as $\delta_{90^\circ}^{ECT}$, as depicted in Fig. 1(b). This definition thus makes strong contact with the widely utilized intercept procedure for stationary crack analysis [5] and, at the same time, approximately incorporating the effect of the extending crack tip on the CTOD value for a growing crack (see, also, Shih et al. [29]). We also note that the amount of crack growth, $\Delta a_t$, shown in Fig. 1(b) represents the distance between the current crack tip and the tip of the initially blunted crack. Here, it is of interest to note that the amount of ductile crack growth should actually be measured from the initial (fatigue) crack tip, not from the blunted tip, such as $\Delta a = \Delta_b + \Delta_t$. However, the mesh arrangement for a symmetric finite element model using cells elements along the crack plane to describe ductile tearing already incorporates an initially blunted crack tip - refer to Section 4.1 and Fig. 7. Since $\Delta_b$ is small, it thus proves convenient for numerical computations to simply measure the amount of crack growth from the blunted tip thereby assuming $\Delta a \approx \Delta a_t$.

## 3. Experimental program

This section describes key details of experimental fracture tests conducted on weld centerline notched SE(T) specimens extracted from girth welds made of different pipe steel grades. Conducted as part of a collaborative research program between the University of São Paulo (USP) and Petrobras, testing of these specimens focused on the evaluation of crack growth resistance data for pipe girth welds with different levels of weld strength mismatch, including a dissimilar welded specimen extracted from a clad line pipe. The experimental program covered: 1) an API 5L X80 [30] high strength, pipeline steel girth weld; 2) a girth weld of a typical C-Mn pipe

internally clad with a nickel–chromium corrosion resistant alloy (CRA) made of ASTM UNS N06625 Alloy 625 [31,32]; and 3) a girth weld made of a typical ASTM A106 Gr C [33] carbon steel pipe. The experimental results described here are used to develop improved $J$-CTOD relationships for the tested materials and, at the same time, to characterize the CTOD for extending cracks based on detailed analyses of stable crack growth for V-grooved weld models.

### 3.1. X80 pipe girth weld

Mathias et al. [4] performed unloading compliance (UC) tests at room temperature of clamped SE(T) fracture specimens for a girth weld made of an API 5L X80 grade pipeline steel [30]. The tested weld joint was made from a 20-inch (508 mm) pipe with thickness, $t =$ 19 mm, using the FCAW process in the 1G (flat) position with a single V-groove configuration in which the root pass was made by GMAW welding. The weld centerline notched specimen illustrated in Fig. 2(a) has fixed overall geometry and crack length to width ratio defined by $a/W = 0.4$ and $H/W = 10$ with thickness $B = 14.8$ mm and width $W = 14.8$ mm. Here, $a$ is the crack depth, $W$ is the specimen width and $H$ is the specimen length ("daylight") between grips. Fig. 2(b) shows the weld groove configuration in which a single bevel design was used in the preparation of the test girth weld. Mechanical tensile tests conducted at room temperature (20°C) using subsize test specimens (6.5 mm gage diameter) provide the engineering stress–strain response for both the baseplate (BM) and weld metal (WM) displayed in Fig. 3(a). Table 1 shows the average tensile properties for the tested girth weld in which the measured yield stress values reveal that the weldment overmatches the baseplate material by 18% at room temperature. The table also includes the strain hardening exponents estimated on the basis of API 579 [34] corresponding to the Ramberg–Osgood model [5,35] to describe the stress–strain behavior for these materials.

The $J$-resistance evaluation procedure followed the test method for clamped SE(T) specimens developed at USP [36] and summarized in recent review article [13]. The methodology builds upon an incremental procedure to evaluate $J$ incorporating a crack growth correction of the measured load–displacement data to obtain accurate estimates of $J$-values with increased crack extension (see also Cravero and Ruggieri [23]). Records of load vs. crack mouth opening displacements (CMOD) were obtained using a clip gage mounted on knife edges attached to the specimen surface. The fracture specimens were first fatigue precracked in bending and then subsequently side-grooved to a net thickness of ~85% of the overall thickness (7.5% side-groove on each side) to promote uniform crack growth. Fig. 4(a) displays the measured resistance curves for the tested X80 girth weld. These fracture data were obtained using specific expressions for factors $\eta$ defined by Eqs. (11) and (12) presented later in Section 5.1. These $\eta$-factors are derived from 2D plane-strain numerical analyses of V-grooved weld models for the clamped SE(T) geometry and incorporate the measured tensile properties for the weld metal and baseplate material. Here, we note that, because of the elastic character of the compliance functions to estimate the current crack length, there is no further need for developing a new set of compliance expressions for the present test weld configuration and, thus, the compliance equations provided by Souza and Ruggieri [37] are employed. Details of the numerical analyses performed to determine a specific set of $\eta$-factors for the tested weld centerline notched specimens are also provided in Sections 4.2.

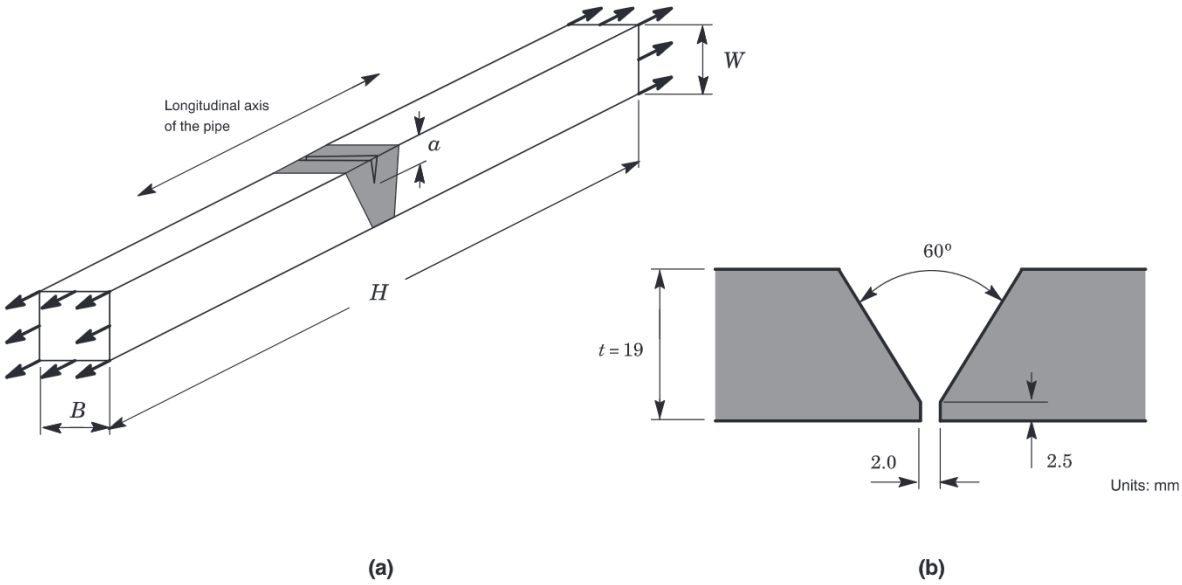


**Fig. 2.** (a) Geometry of tested clamped SE(T) specimens for the API X80 pipeline girth weld with weld centerline notch having $a/W = 0.4$, $H/W =$ 10 and $B \times B$ configuration. (b) Single bevel configuration used in the preparation of the test girth weld.

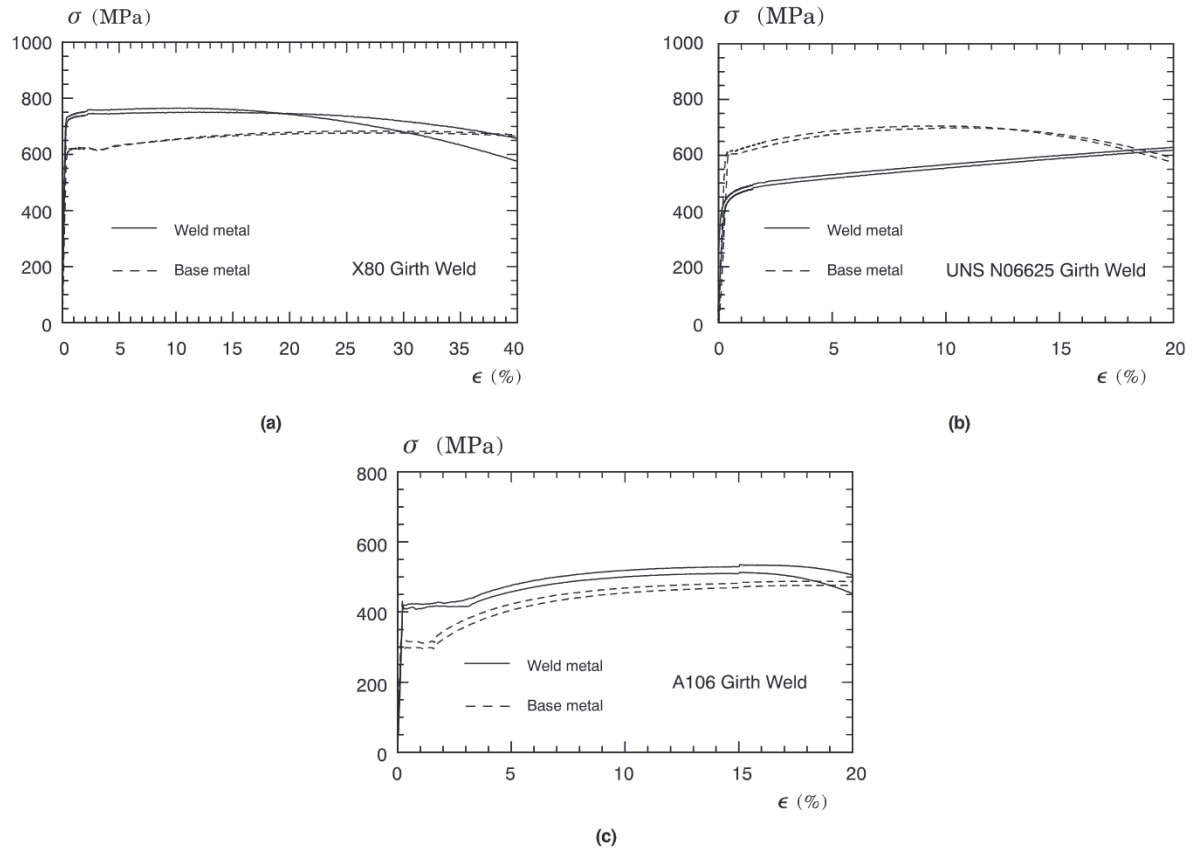


**Fig. 3.** Engineering stress–strain data for the tested girth welds at room temperature: (a) API X80. (b) UNS N06625 alloy. (c) ASTM A106 Gr C.

**Table 1**
Tensile properties for the tested girth welds, including the baseplate material, in which $\sigma_{ys}$ is the yield stress (0.2% offset method), $\sigma_{uts}$ is the tensile strength and $n$ is the strain hardening exponent derived from API 579 [34].

| Girth Weld Material | | $\sigma_{ys}$ (MPa) | $\sigma_{uts}$ (GPa) | $E$ | $\sigma_{uts}/\sigma_{ys}$ | $n$ |
|---|---|---|---|---|---|---|
| API X80 | BM | 609 | 679 | 209 | 1.11 | 20.3 |
| | WM | 716 | 750 | 215 | 1.05 | 35.2 |
| UNS N06625 | BM | 620 | 700 | 200 | 1.13 | 18.9 |
| | WM | 462 | 627 | 158 | 1.36 | 9.7 |
| ASTM A106 | BM | 308 | 482 | 215 | 1.66 | 7.1 |
| | WM | 415 | 524 | 185 | 1.26 | 11.8 |

### 3.2. Dissimilar Nickel–Chromium girth weld

Sarzosa et al. [38] conducted fracture resistance tests based on the UC method at room temperature on weld centerline notched SE(T) specimens extracted from a girth weld of a typical API 5L X65 pipe internally clad with a nickel–chromium corrosion resistant alloy (CRA) made of UNS N06625 alloy 625 [31,32], also commercially known as Inconel 625 alloy. The tested weld joint was made from an 8-inch pipe (203 mm outer diameter) having overall thickness, $t = 19$ mm, which includes a clad layer thickness, $t_c = 3$ mm. Girth welding of the pipe was performed using 100% $CO_2$ gas-shielded FCAW process in the 5G (horizontal) position with a single V-groove configuration in which the root pass was made by TIG welding in the 2G (vertical) position. The fracture specimen shown in Fig. 5(a) has $a/W = 0.3$ and $H/W = 10$ with thickness $B = 16$ mm, width $W = 16$ mm and $H = 160$ mm with 7.5% side-groove on each side. Fig. 5(b) depicts the single bevel configuration employed in the preparation of the dissimilar girth weld. A nickel–chromium filler metal matching the UNS N06625 Alloy 625 [31,32] was utilized to produce the girth weld and, thus, the clad internal layer and the weld metal have essentially the same mechanical properties. Fig. 3(b) shows the engineering stress–strain curves for both materials from which the average tensile properties for the tested girth weld are presented in Table 1. Here, the measured tensile properties indicate that the weld material undermatches the baseplate material by ≈ 25% at room temperature and exhibits a strong linear hardening behavior, which contrasts sharply to the hardening properties of the X65 pipe material.

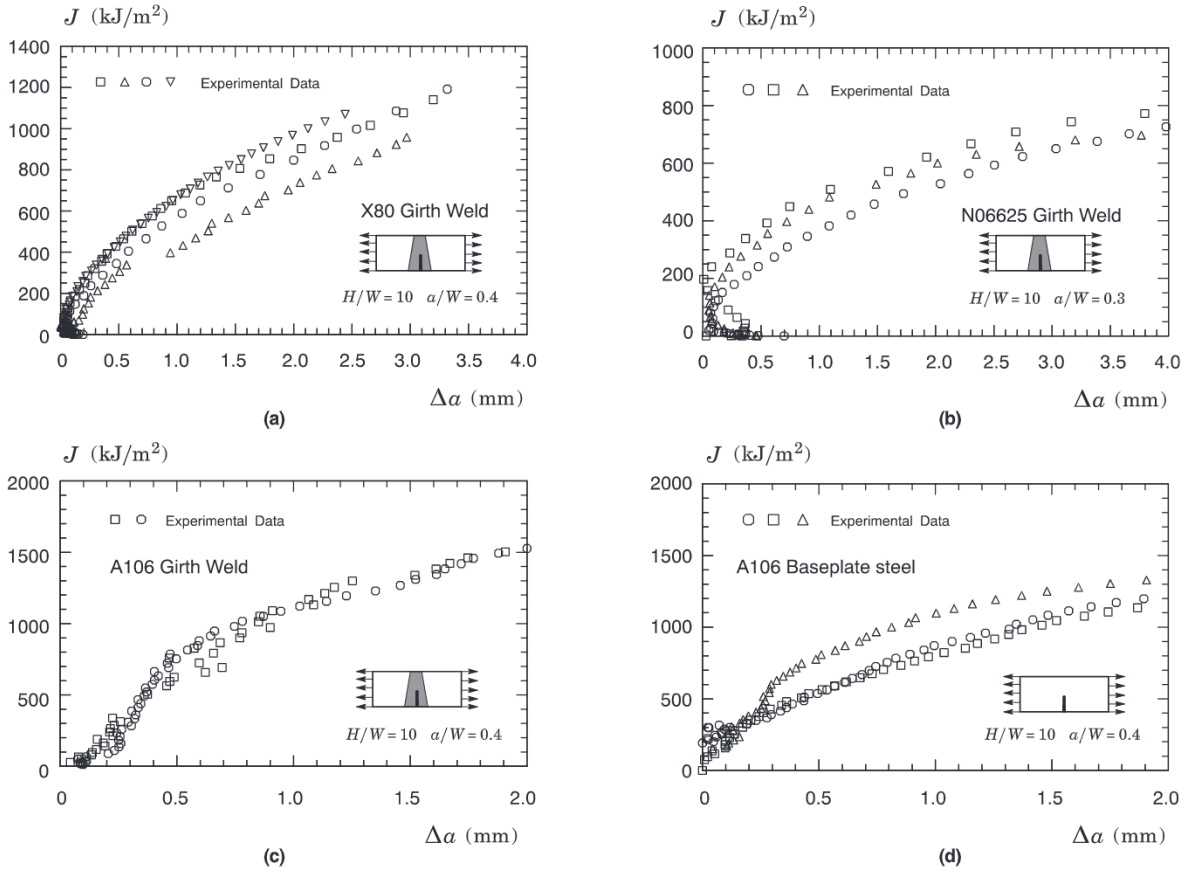


**Fig. 4.** *J*-resistance curves including crack growth correction for the clamped SE(T) specimens extracted from the tested girth welds: (a) API X80. (b) UNS N06625 alloy. (c) ASTM A106 Gr C girth weld. (d) ASTM A106 Gr C baseplate.

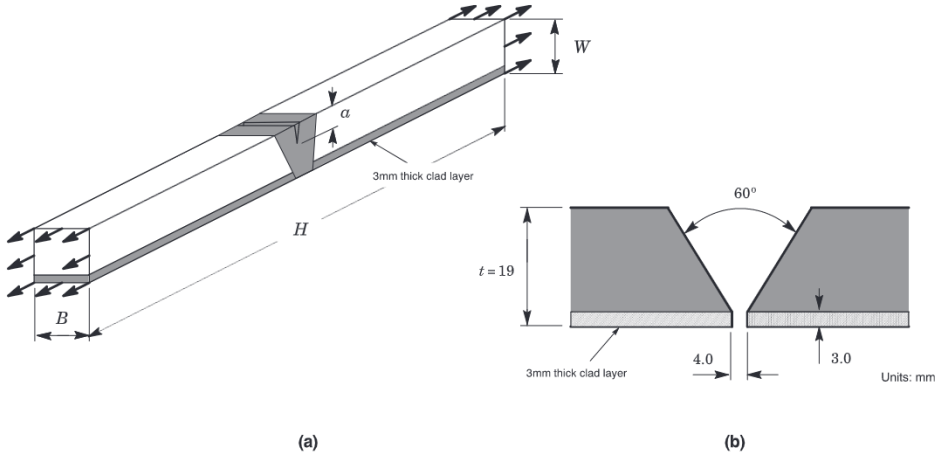


**Fig. 5.** (a) Geometry of weld centerline notched SE(T) specimens for the dissimilar nickel–chromium girth made of UNS N06625 Alloy [31,32] having $a/W = 0.3$, $H/W = 10$ and $B \times B$ configuration. (b) Single bevel configuration used in the preparation of the dissimilar test girth weld.

Experimental evaluation of $J - \Delta a$ data followed similar test protocol as already previously outlined for the API X80 girth weld with $\eta$-factors also given by Eqs. (11) and (12) given next in Section 5.1. Further, to evaluate the CTOD using the DCG method, Sarzosa et al. [38] equipped an additional fracture specimen with a double clip-gage fixture as required for CMOD measurements at two different points illustrated in Fig. 3(b) - presentation of the CTOD $-R$ curve obtained by Sarzosa et al. [38] is postponed until Section 5.2.3. Fig. 4(b) displays the *J*-resistance curves for the tested dissimilar nickel–chromium girth weld. Apart from a "crack backup" behavior,

generally associated with an increase in specimen stiffness with increased loading [3,39,40], in the early part of the $J-R$ curve for all tested configurations, only relatively small scatter is observed in the fracture resistance data.

### 3.3. A106 pipe girth weld

Ferreira et al. [41] have carried out a series of fracture experiments for a girth weld made of a typical ASTM A106 Gr C [33] carbon steel pipe to measure its ductile tearing properties based on the UC method at room temperature. The tested weld joint was made from a 9-inch nominal size with 244 mm outer diameter and wall thickness, $t = 23$ mm. Girth welding of the pipe was performed using shielded metal arc welding (SMAW) process in the 1G (flat) position with a single V-groove configuration in which the root pass was made by TIG welding in the same 1G (flat) position. The pipe was rotated continuously to maintain this position and, further, to ensure similar levels of heat input along the entire girth weld. The filling electrode with low hydrogen coating (AWS E7018) was chosen to provide a degree of weld strength overmatch higher than the usual levels of overmatch for girth welds of pipelines made of high strength steels, such as grades greater than API X70 and X80. Post weld heat treatment (PWHT) of the tested weld joint was conducted by heating it to 620 °C for 1 h followed by cooling down to 300 °C in a heat treat furnace and then left to cool in air to relieve the residual stresses that were potentially introduced during the girth welding.

With very minor differences, the UC test procedure followed the same test methodology already outlined for testing the other girth weld materials. Here, the weld centerline notched SE(T) specimens with end-clamped conditions were extracted from the longitudinal direction of the pipe specimen illustrated in Fig. 2 to measure tearing resistance properties in terms of $J-\Delta a$ curves using the $\eta$-factors described by Eqs. (11) and (12) provided in Section 5.1. Further, to assess the influence of weld strength mismatch on the fracture resistance properties, UC fracture tests at room temperature were also performed on clamped SE(T) specimens made of the pipe material also extracted from the longitudinal direction of the pipe specimen. The tested geometries have similar configuration to the specimen shown in Fig. 2(a) with $a/W = 0.4$, thickness $B = 20$ mm, width $W = 20$ mm and $H = 200$ mm ($H/W = 10$). The single bevel design used in the preparation of the test girth weld is also similar to the weld groove configuration shown in Fig. 2(b) but with slightly larger root opening of 6 mm and a smaller root face of 2 mm. Standard tensile tests conducted on conventional tensile specimens provided the mechanical properties at room temperature (20°C) for the tested materials. The specimens for the pipe material were extracted from the longitudinal direction of the pipe whereas the specimens for the weld metal were machined from the deposited weld metal with their longitudinal axes parallel to the welding direction. Table 1 provides the average tensile properties of the baseplate material and the weld metal. The measured values indicate that the weldment overmatches the baseplate material by 35% at room temperature.

We first draw attention to the load carrying capacity for the homogeneous and weld centerline notched configurations. Fig. 6(a-b) shows typical measured load–displacement curves (as described by CMOD) for both material conditions. The effect of weld overmatching on the applied load is evident in this plot. At similar levels of crack mouth opening displacement, the applied load for the welded specimen increases approximately by 20% compared to the load response for the homogeneous geometry. Fig. 4(c-d) display the crack growth resistance curves obtained in the experimental study and illustrate the effects of weld strength mismatch on the fracture resistance properties for the tested materials. Consider first the crack growth results for the welded specimen displayed in Fig. 4(c), in which, despite some inherent scatter in the measured data, the resistance curves increase sharply in the early part of the resistance curve ($\Delta a \leq 0.5$ mm) and then show some sign of a constant tearing modulus reaching large $J$-values with only moderate amounts of tearing thereby typifying a tough material. Consider next the fracture resistance data for the pipe material shown in Fig. 4(d). While these curves also exhibit some inherent scatter in the measured data, these resistance curves are somewhat lower than the corresponding $J-\Delta a$ data for the girth weld material for the entire range of measured ductile tearing. For example, at the amount of

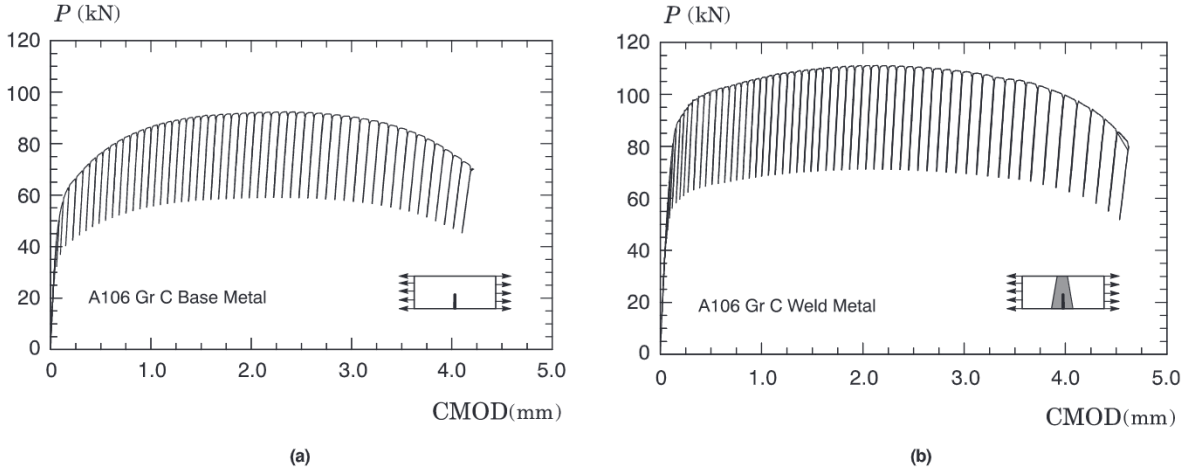


**Fig. 6.** Measured load-CMOD curve for the A106 girth weld using clamped SE(T) specimens with $a/W = 0.4$: (a) Pipe material. (b) Girth weld with 35% weld strength overmatch.

crack growth, $\Delta a = 2$ mm, the corresponding value of the $J$-integral is ~1500 kJ/m$^2$ for the pipe girth weld whereas the corresponding $J$-value is ~1200 kJ/m$^2$ for the pipe material.

## 4. Numerical procedures and finite element models

### 4.1. Computational cell approach for ductile tearing: the GTN model

This section repeats key concepts already introduced in previous work of Xia and Shih [42], Ruggieri and Dodds [43] and Gullerud et al. [44] to provide a summary of the cell-based framework to model stable crack growth in ductile materials as required to develop improved CTOD resistance data for a growing crack. In the context of the present work, ductile fracture in metals is characterized as a process of material failure which incorporates various and simultaneous micromechanisms [45]. The commonly observed stages of this process at the microscale level are: a) formation of a void at an inclusion or second phase particle by either decohesion or particle cracking; b) growth of the void around the particle by means of increased plastic strains and hydrostatic stresses and c) coalescence of the growing void with other adjacent voids. Experimental observations and computational studies show that the plastic strains for nucleation are small thereby causing only little damage in the material ahead of the crack tip. This feature enables simplification of the ductile failure process by assuming the growth of microvoids as the critical event controlling ductile extension.

Motivated by the above observations, Xia and Shih [42] proposed a phenomenologically-based model using computational cells to include a realistic void growth mechanism and a microstructural length-scale physically coupled to the size of the fracture process zone. Void growth remains confined to a layer of material symmetrically located about the crack plane, as illustrated in Fig. 7(a), and having thickness $D$, which is associated with the mean spacing of the larger, void initiating inclusions. Fig. 7(b) illustrates the typical mesh arrangement for a symmetric finite element model; here the cells (elements) along the crack plane have a square cross section with specified height $D/2$ and contain a cavity of initial volume fraction $f_0$ (the initial void volume divided by cell volume). As a further simplification, the void nucleates from an inclusion of relative size $f_0$ immediately upon loading. Progressive void growth and subsequent macroscopic material softening in each cell are described with the Gurson-Tvergaard (GT) constitutive model for dilatant plasticity [46,47] given by

$$\left(\frac{\sigma_e}{\widetilde{\sigma}}\right)^2 + 2q_1 f \cosh\left(\frac{3q_2\sigma_m}{2\widetilde{\sigma}}\right) - \left(1 - q_3 f^2\right) = 0 \tag{8}$$

where $\sigma_e$ denotes the effective Mises (macroscopic) stress, $\sigma_m$ is the mean (macroscopic) stress, $\widetilde{\sigma}$ is the current flow stress of the cell matrix material and $f$ defines the current void fraction. Factors $q_1, q_2$ and $q_3 = q_1^2$ introduced by Tvergaard [47] improve the model predictions for periodic arrays of cylindrical and spherical voids. In the analyses addressed later for the tested girth welds, improved $q$-values derived from the work of Faleskog and Shih [48] are used; these $q$-values are applicable to a wide range of material flow properties (strain hardening properties and yield stress) for common pressure vessel and structural steels.

A characteristic feature of the GT model and associated yield function given by previous Eq. (8) is its rather poor description to predict material failure under conditions of low stress triaxiality. Such conditions exist in tensile loaded specimens including specifically the clamped SE(T) configurations analyzed here. To improve the response of the GT model under low triaxiality conditions, the strain-controlled acceleration of void growth proposed by Chu and Needleman [49] provides an approximate additional contribution to the void growth, denoted $df_n$, by considering the nucleation of new, secondary voids from smaller inclusions in the cell matrix material during the coalescence phase caused by large plastic strains in the form

$$df_n = \frac{f_N}{s_N\sqrt{2\pi}} \exp\left[-\frac{1}{2}\left(\frac{\bar{\varepsilon}_p - \epsilon_N}{s_N}\right)\right] \tag{9}$$

where it is understood that the plastic strain at nucleation of new voids, $\bar{\varepsilon}_p$, follows a normal distribution with a mean value $\epsilon_N$, a standard deviation $s_N$ and a volume fraction of void nucleating particles given by $f_N$. When the above strain-controlled void growth is used in conjunction with Eq. (8), the resulting damage framework is commonly referred to as the GTN model. Besson [50] provides a

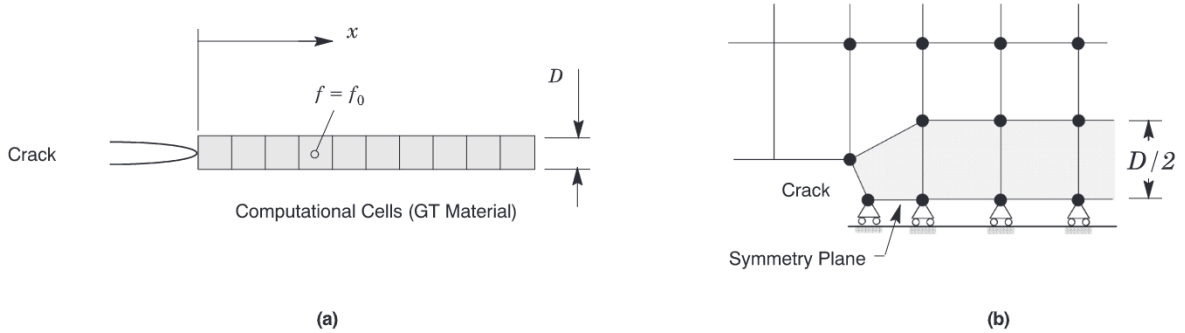


**Fig. 7.** Computational cell model for Mode I ductile tearing picturing the schematic path of a growing crack in a ductile material.

comprehensive review article on continuum models to describe fracture in ductile materials.

Section 5.2.1 addresses calibration of the key cell parameter, $f_0$, using experimentally measured $J-\Delta a$ curves obtained from testing the clamped SE(T) specimens for the girth welds under consideration in the present study. The calibration process also includes appropriate choices of the parameters defining the strain nucleation model given by the above Eq. (9). In general, it becomes more convenient to fix the cell size, $D/2$, and parameters $f_N$ and $s_N$ at the onset of the analysis and calibrate the key parameter $\in_N$ as several hundred times greater than the yield strain value for the material (typical values for $\in_N$ range from $300\in_0$ to $600\in_0$ where $\in_0$ defines a reference yield strain [43]) such as the onset of strain-controlled nucleation occurs well beyond the attainment of peak stress in the cells where damage takes place. Despite some ambiguity in specifying values for $f_N, s_N$ and $\in_N$, inclusion of void growth due to the formation of new voids does improve the applicability of the cell constitutive model. Ruggieri and Dodds [43] discuss this issue and provide further studies of the strain nucleation parameters for a single cell model.

### 4.2. Finite element models for stationary crack analysis

Development of a specific set of $\eta$-factors and $J-$CTOD relationships more applicable to the tested weld centerline crack configurations require numerically determined solutions generated from V-groove weld models. Nonlinear finite element analyses are described for plane-strain models of clamped SE(T) fracture specimens with fixed clamp distance over specimen width ratio, $H/W = 10$, and varying crack sizes, as characterized by $a/W$-ratios in the range 0.2–0.7 with increments of 0.1. Here, the specimen width, $W$, is defined by each tested geometry as previously described. Moreover, these plane-strain models incorporate the geometry of the weld groove configuration used in the preparation of the test girth weld presented in Section 3. Fig. 8(a) shows the 2-D finite element models constructed for the plane-strain analyses of the clamped SE(T) specimen with stationary crack having $a/W = 0.4$ for the X80 test geometry. This model incorporates the V-groove weld configuration shown in Fig. 2(b). With minor differences, all other crack models have very similar features. Further, the plane-strain model of the fracture specimen for the UNS N06625 test geometry also includes the 3 mm clad layer as indicated in Fig. 5. A small key-hole at the crack tip having a radius, $\rho_0$, of 2.5 μm is employed to enhance resolution of near-tip stresses and strains, as well as computation of $J$-values at low deformation levels. Symmetry conditions permit modeling of only one-half of the specimen with appropriate constraints imposed on the symmetry as well as plane-strain constraints ($w = 0$) imposed on each node, as indicated in Fig. 8. In particular, clamped grip conditions are enforced by imposing zero lateral displacements at the end of the specimens as also indicated in Fig. 8(a). A typical half-symmetric, 2-D model has one thickness layer of 2000–3000 elements and 4000–6000 nodes depending on the geometry, crack size and groove details. These numerical models are loaded by

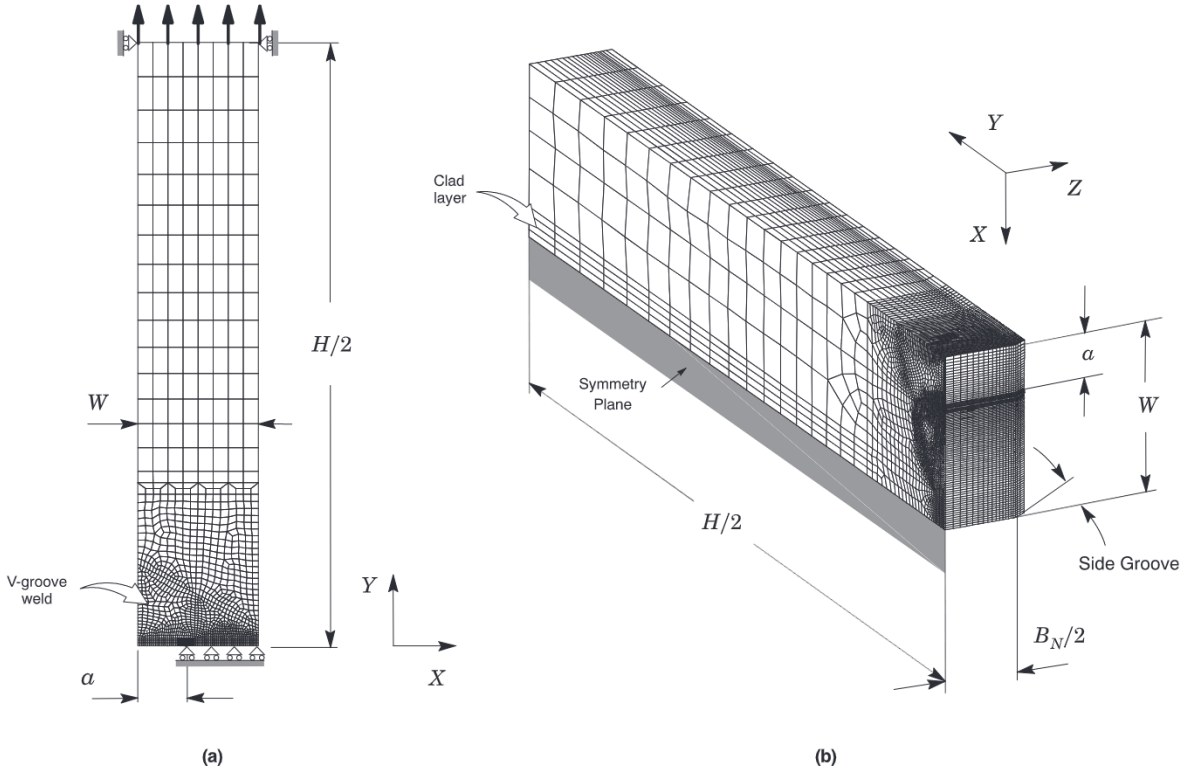


**Fig. 8.** Typical finite element models for stationary crack analysis of the clamped SE(T) specimen incorporating the V-groove weld configuration: (a) Plane-strain model for the X80 girth weld test geometry with $a/W = 0.4$. (b) 3-D numerical model for the UNS N06625 girth weld test geometry with $a/W = 0.3$.

displacement increments imposed on the loading points to enhance numerical convergence with increased levels of deformation.

Section 5.2.3 describes 3-D numerical analysis of ductile crack growth for the dissimilar nickel–chromium girth weld made of UNS N06625 alloy 625 in which the experimental $J-\Delta a$ data are also determined from improved $\eta$-factors derived from 3-D stationary crack analysis. These 3-D finite element models have $H/W = 10$ and varying crack sizes, as characterized by $a/W$-ratios in the range 0.2–0.7 with increments of 0.1. Fig. 8(b) shows the quarter-symmetric, 3-D model for the clamped SE(T) specimen having $a/W = 0.3$ in accordance with the UNS N06625 test geometry, including the 3 mm clad layer indicated in Fig. 5. The finite element mesh has 15 variable thickness layers defined over the half net thickness $(B_N/2)$ to accommodate strong $Z$ variations in the stress distribution and at the same time to resolve the pointwise $J$-integral over the crack front. Here, the layer thickness defining the specimen center plane at $Z = 0$ is $0.055B_N$ whereas the layer defined near the side-groove $(Z = B_N/2)$ is $0.015B_N$. The additional 3 outermost layers describing the side-groove region then compose the full bulk of the specimen, $B/2$, as indicated in Fig. 8(b). The quarter-symmetric, 3-D model for this specimen also incorporates an initially blunted crack tip with radius, $\rho_0$, of 2.5 μm and has ~61,800 nodes and ~56,000 8-node, 3-D elements.

### 4.3. Finite element models for growth analysis

Nonlinear finite element analyses incorporating crack growth are also described for the plane-strain models of the tested specimens having the geometries described in Section 3. Fig. 9(a) shows the finite element model constructed for the 2-D analyses of the SE(T) geometry having $a/W = 0.3$ employed in the fracture testing of the UNS N06625 girth weld. The numerical model also incorporates the V-groove weld configuration and the 3 mm clad layer shown in Fig. 5. To simulate ductile crack extension using the GT model, the planar mesh (2-D) for this configuration contains a row of 112 computational cells, each cell with size $D/2 = 100$ μm, along the remaining crack ligament $(W-a)$ as depicted in the arrangement of Fig. 7(b). The choice of the cell size, $D/2$, follows Ruggieri and Dodds [43] on the basis of an approximate correlation of spacing between the large inclusions and the crack tip opening displacement (CTOD) at the onset of macroscopic crack growth in conventional fracture specimens for common pressure vessel steels. Symmetry conditions permit modeling of only one-half of the specimen with appropriate constraints imposed on the remaining ligament. This half-symmetric, plane-strain model is similar to the previous numerical model employed in the stationary crack analyses previously described and has one thickness layer of 1778 elements and 3790 nodes with plane-strain constraints $(w = 0)$ imposed on each node. Further, to evaluate the CTOD during crack extension based on the DCG procedure, the finite element model is equipped with a rigid, elastic element at the crack mouth as indicated in Fig. 9(a). This arrangement thus enables the measurements of crack opening displacements (COD) at two different points as required in the DCG method (refer to Section 2.2). Again, all other numerical models for growth analyses have very similar features.

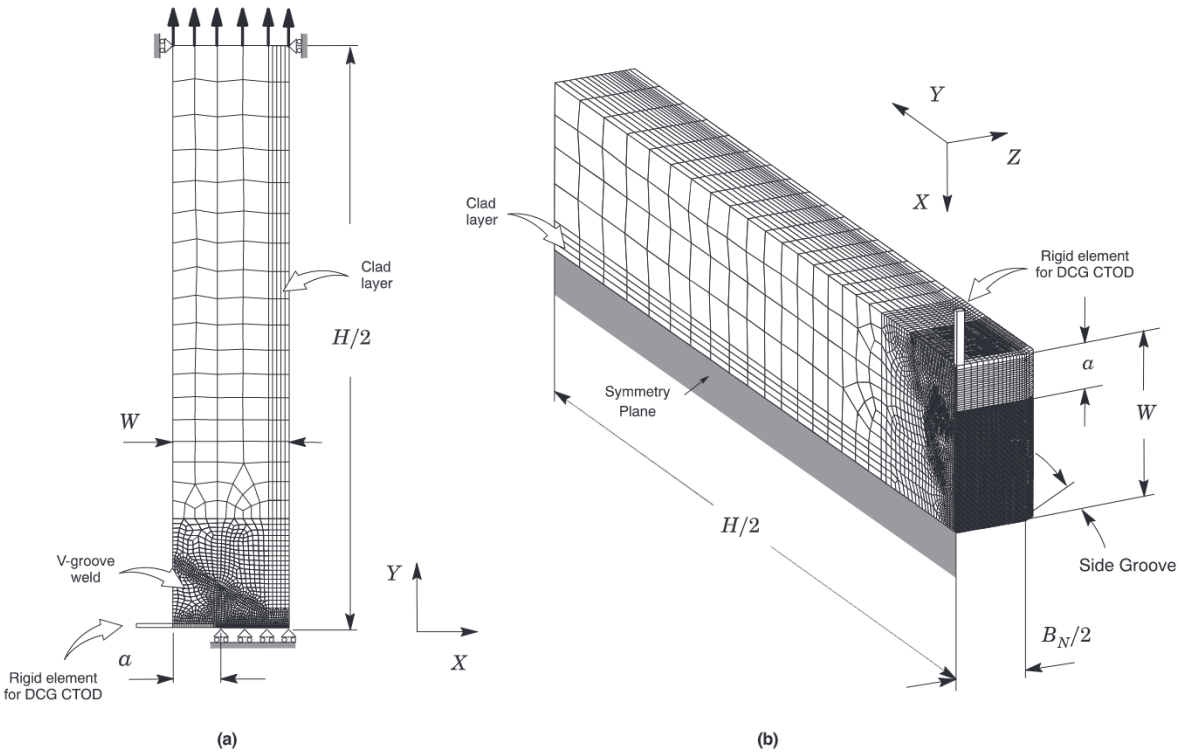


**Fig. 9.** Finite element models for the clamped SE(T) specimens with $a/W = 0.3$ employed in the fracture testing of the UNS N06625 girth weld: (a) Half-symmetric plane-strain model. (b) Quarter-symmetric 3-D numerical model.

Experimental observations of low-constraint fracture specimens employed in $J$-resistance testing of ductile material often reveal a rather severe crack front tunneling, even in side-grooved configurations, which contrasts sharply to the uniform growth implicitly assumed in the plane-strain analysis considered in the present study. To address this issue, 3-D finite element analyses incorporating ductile crack growth are also performed on the dissimilar UNS N06625 alloy 625 girth weld to examine 3-D effects on the resulting CTOD resistance curve for this test configuration. Fig. 9(b) displays the quarter-symmetric 3-D finite element model for the tested clamped SE(T) specimen with $a/W = 0.3$ and the V-groove weld geometry - the numerical model also incorporates the 3 mm clad layer and a rigid, elastic element at the crack mouth to measure the DCG CTOD as indicated in the figure. The 3-D mesh is thus obtained by simply extruding the 2-D mesh along the Z-axis; the in-plane $(X-Y)$ finite element mesh has therefore identical mesh refinement as the plane-strain model, including a row of 112 computational cells, each cell with size $D/2 = 100$ μm, along the remaining crack ligament $(W-a)$. This finite element mesh has 15 variable thickness layers defined over the half net thickness $(B_N/2)$ and same layer thickness at the specimen center plane and at the side groove region as the numerical model employed in the stationary crack analyses previously described. The mesh arrangement at $Y = 0$ contains a *slab* of $15 \times 112 = 1680$ cell elements to capture the onset of ductile tearing and crack growth along the crack front on the specimen centerplane.

### 4.4. Material models and finite element procedures

The finite element solutions reported here are generated by employing an elastic–plastic material model incorporating conventional Mises plasticity theory in small geometry change (SCG) setting for the stationary crack analyses and large geometry change (LCG) setting for the crack growth analyses. The material model for both the weld metal and baseplate material utilizes a piecewise-linear representation of the true stress-logarithm strain behavior derived from the measured tensile response for each material described in Fig. 3 and Table 1 with a Poisson's ratio, $\nu = 0.3$. The finite element code WARP3D [51] provides the numerical solutions for the extensive simulations reported here including stationary and crack growth analyses implementing the cell model. The research code FRACTUS2D [52] is employed to compute the required $\eta$-factors and the $J-$CTOD relations derived from stationary and growing analyses for the analyzed fracture specimens incorporating a V-groove weld. Evaluation of the numerical value of CTOD follows the 90° procedure [5] to the deformed crack flanks as illustrated in Fig. 1(b).

The local value of the mechanical energy release rate at a point along the crack front is given by [53]

$$J = \lim_{\Gamma \to 0} \int_{\Gamma} \left[ W_s n_1 - \sigma_{ij} \frac{\partial u_i}{\partial x_1} n_j \right] d\Gamma \tag{10}$$

where $\Gamma$ denotes a contour defined in a plane normal to the crack front on the undeformed configuration beginning at the bottom crack face and ending on the top face, $n_j$ is the outward normal to $\Gamma$, $W_s$ denotes the stress-work density per unit of undeformed volume, $\sigma_{ij}$ and $u_i$ are Cartesian components of stress and displacement in the crack front coordinate system. The finite element computations employ a domain integral procedure [53] for numerical evaluation of Eq. (10) to provide pointwise and front average values of $J$ across the crack front at each loading level. In each case, the $J$-values are computed over domains defined outside material having the highly non-proportional histories of the near-tip fields and thus retain a strong domain (path) independence. Moreover, the thickness average values of $J$ agree very well with estimation schemes based upon $\eta$-factors for deformation plasticity [5] so that they provide a convenient parameter to characterize the average intensity of far field loading on the crack front.

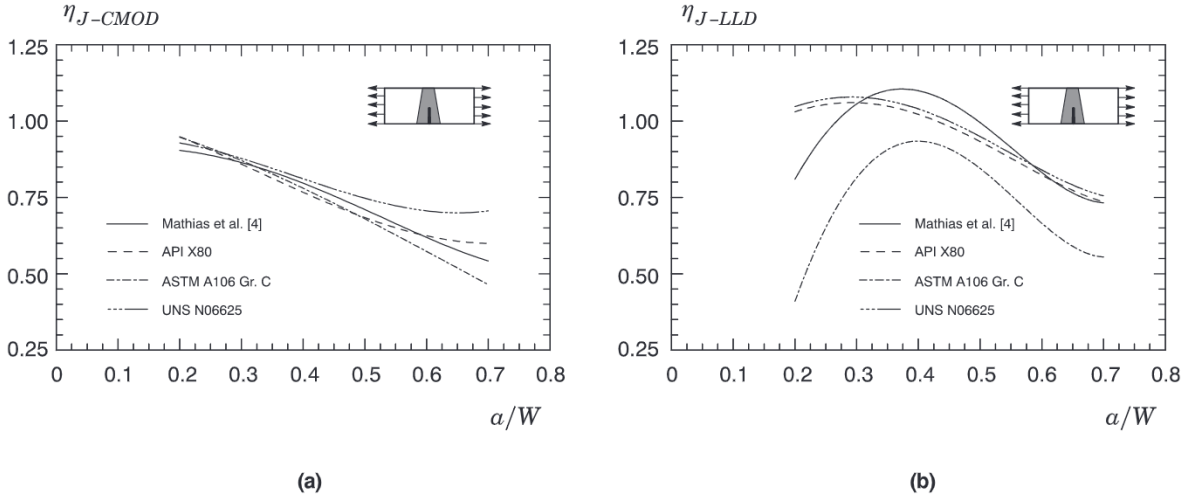


**Fig. 10.** Dependence of $\eta$-factors on $a/W$-ratio derived from plane-strain analysis incorporating the weld groove configuration and material properties for the tested girth welds: (a) Factors $\eta$ based on CMOD. (b) Factors $\eta$ based on LLD.

## 5. Results

### 5.1. $\eta$-factors and $J$ –CTOD relationships for stationary crack analysis of V-groove welds

The crack growth resistance curves discussed in Section 3 were obtained using $\eta$-factors derived from finite element analysis of plane-strain models incorporating the weld groove configuration and the material properties described in Section 4.2. Fig. 10(a-b) provides factors $\eta_{J-CMOD}$ and $\eta_{J-LLD}$ for the weld centerline notched SE(T) specimens with varying $a/W$-ratios for all girth welds under consideration. In these plots, the lines represent fitting curves to the computed plane-strain $\eta$-values as presented next. For comparison, the figures also include the $\eta$-factor solutions for homogeneous clamped SE(T) geometries derived from previous work of Mathias et al. [4].

Consider first the $\eta_{J-CMOD}$ results shown in Fig. 10(a). Apart from small differences, the $\eta$-values for the girth welds are in close agreement with the results of Mathias et al. [4] in the range $0.2 \leqslant a/W \leq 0.4$–0.5. In contrast, the $\eta$-values depend somewhat more sensitively on the girth weld material, particularly for the UNS N06625 girth weld with $a/W \geqslant 0.5$. Here, these larger differences in the $\eta$-values most likely arise from the much stronger influence of the V-shaped weld groove in connection with the level of mismatch in material properties on the load-CMOD curve and, thus, on the plastic area upon which $\eta_J$ is defined. As the crack size increases towards the weld root region, the local width of the weld metal effectively affecting the crack tip is narrower (refer to Fig. 2) so that the effects of strength mismatch on the evolution of load with CMOD are diminished. Overall, however, these differences are not large enough to significantly influence the determination of $J$ based on the plastic area under the load-CMOD curve.

Consider next the $\eta_{J-LLD}$ results shown in Fig. 10(b). A different picture emerges here as the $\eta$-values for the girth welds display larger differences relative to the results of Mathias et al. [4]. Remarkably, the $\eta$-values for the A106 girth weld are substantially lower compared to the results for homogeneous material over the entire $a/W$-ratio considered. While we have not explored in details such behavior, it can be understood by the following argument. This girth weld has a very high degree of strength mismatch between the weld metal and the baseplate material of $\approx 35\%$, thus shielding the weld region from the (remote) applied displacements at the clamped ends. While the CMOD is less affected by the degree of mismatch in material properties, it becomes clear that the LLD is much more sensitive to the strength of the weld metal relative to the baseplate. Similar results were also found in recent work of Paredes and Ruggieri [11] who investigated the effects of weld strength mismatch on $\eta$-factors for weld centerline notched SE(T) configurations having square groove welds. However, since $\eta_{J-LLD}$ enters into the fracture resistance evaluation procedure only to correct $J$ for crack growth (refer to Section 2.1), it is expected to give only a relatively moderate effect on the $J$-resistance curves.

The $J$ –CTOD relationships for the stationary crack analysis of V-groove weld models are also of interest. Fig. 11 shows the variation of $m = J/(\delta\sigma_f)$ with varying $a/W$-ratios, as described by open symbols, for the V-groove weld models of the tested girth welds. For every material considered in Fig. 11, parameter $m$ exhibits a weak dependence on the $a/W$-ratio. As expected, though, the $m$-value displays a more noticeable sensitivity on material properties, ranging from ~1.2 for the UNS N06625 girth weld to 1.4–1.5 for the X80 girth weld. For reference, this plot also includes the dependence of $m$ on crack size over the range $0.2 \leqslant a/W \leq 0.7$ obtained from Eq. (14) appearing in previous work of Sarzosa et al. [28], hereafter referred to as SSR, with the strain hardening exponent for the weld metal material given in Table 1. Relative to the results of SSR, which are applicable to stationary crack analyses of plane-sided specimens made of homogeneous material, the present set of $m$-values derived from the V-groove weld models is in generally good agreement.

Now, to provide a simpler manipulation of the previous results, a functional dependence of factors $\eta_J$ and parameter $m$ with $a/W$-ratio is obtained in the form

$$\eta_{J-CMOD} = b_0 + b_1(a/W) + b_2(a/W)^2 + b_3(a/W)^3 \tag{11}$$

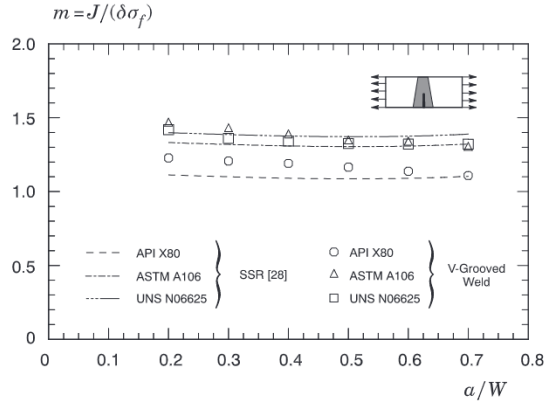


**Fig. 11.** Dependence of $J$ –CTOD relationships, as characterized by parameter $m$, on $a/W$-ratio derived from plane-strain analysis incorporating the weld groove configuration and material properties for the tested girth welds.

$$\eta_{J\_LLD} = c_0 + c_1(a/W) + c_2(a/W)^2 + c_3(a/W)^3 + c_4(a/W)^4 + c_5(a/W)^5 \tag{12}$$

$$m = d_0 + d_1(a/W) + d_2(a/W)^2 + d_3(a/W)^3 \tag{13}$$

which are applicable in the range of $0.2 \leqslant a/W \leq 0.7$ for stationary cracks. Tables 2,3 provide the coefficients of the above polynomial fitting for the tested girth welds considered in the present study.

### 5.2. CTOD resistance data for extending cracks

#### 5.2.1. Numerical simulation of crack growth

Numerical simulation of crack growth in plane-strain setting for the SE(T) specimens described here begins with calibration of the cell model parameters for the girth welds employed in this study. Guided by the previous studies of Ruggieri and Dodds [43], Gullerud et al. [44] and Ruggieri and Dotta [54], the analysis follows from matching the computed resistance curves with the measured fracture resistance data. Since the GTN constitutive model depends on a number of parameters, the model calibration can be accomplished in several ways. As already briefly discussed in preceding sections, the simplest approach is to fix the cell size, $D/2$, and, further, the strain nucleation parameters $f_N$ and $s_N$ at the onset of the analysis and then determine suitable values for the initial volume fraction, $f_0$, and the mean value of the plastic strain driving the nucleation of new voids, $\epsilon_N$, that produce the best fit to the measured crack growth data for the tested specimens. However, while the calibrated values for $f_0$ and $\epsilon_N$ are somewhat coupled (a change in $\epsilon_N$ also leads to a change in $f_0$ that produces the best fit to the measured fracture resistance data), the $f_0$-value that yields the resistance curve in agreement with the experimental results is presumably weakly affected by small changes in $\epsilon_N$ (recall that $\epsilon_N$ can take a value several hundred times greater than the yield strain value for the material).

Fig. 12 shows the predicted $J-\Delta a$ curves for every case under consideration using the cell size $D/2 = 100$ μm, $f_N = 0.5$ and $s_N = 0.05$ and slightly varying $\epsilon_N$-values. For each tested girth weld and the A106 baseplate material, predicted $R$-curves are shown for three values of the initial volume fraction as indicated in the plots. These analyses are rather conclusive as the initial volume fraction, $f_0$, plays a central role in capturing the predicted evolution of $J$ with $\Delta a$ for every case. Consider, for example, the results for the X80 girth weld displayed in Fig. 12(a). For $f_0 = 0.003$, the predicted $R$-curve agrees well with the average measured values for almost the entire range of growth despite the inherent scatter in the experimental data. However, since the primary interest here lies in the description of fracture resistance as a means to determine the CTOD for a growing crack, some differences between the predicted and the measured crack growth resistance curve are not of particular concern. In contrast, the use of $f_0 = 0.01$ produces a lower resistance curve relative to the measured data. Essentially similar behavior is observed for other tested materials, including the A106 baseplate steel pipe. Table 5 summarizes the calibrated GTN parameters and includes factors $q_1$, $q_2$ derived from the work of Faleskog and Shih [48].

#### 5.2.2. CTOD-R curves based on plane-strain analyses

The previous 2-D finite element analyses incorporating a phenomenological model for stable crack growth provide a basis for describing ductile fracture response of the tested girth welds in terms of CTOD $-\Delta a$ data. Here, the CTOD fracture resistance curves displayed in Fig. 13 are determined as follows: (1) CTOD-values based on the double clip gage (DCG) procedure, denoted $\delta_{DCG}$, displayed in Fig. 1(a). (2) CTOD-values determined using the 90° intercept procedure based on the CTOD-values evaluated using the 90° intercept procedure based on the *extending* crack tip and the deformed crack flanks illustrated in Fig. 1(b), $\delta_{ECT}$. (3) CTOD-values converted from corresponding $J$-values of the resistance curves described by the solid line in previous Fig. 12 using the computed $J-$CTOD relationships expressed by Eq. (13) with the coefficients $d_k$ given in Table 4. Here, the computed curves based on the cell model analysis that give the best fit to the corresponding sets of experimentally measured $J-R$ curves are considered as average resistance curves for each case considered. Moreover, the CTOD-resistance curves in which the CTOD-value is converted from the $J-$CTOD relationship for stationary cracks given by Eq. (14) appearing in SSR [28] are also provided to aid in assessing the relative changes in CTOD $-\Delta a$ data based on the previous definitions for CTOD. Further observe that Fig. 13(d) refers to the CTOD resistance curves for the ASTM A106 baseplate material and, thus, only the CTOD $-R$ curve derived from SSR [28] is included in the plot.

The results displayed in Fig. 13 show a dependence of the crack growth resistance curves on the CTOD model adopted. Such dependence also appears to be related to material flow properties and degree of weld strength mismatch. Consider first the fracture resistance results for the X80 and UNS N06625 girth welds shown in Fig. 13(a-b). Here, the variation of CTOD with $\Delta a$ using the $J-$CTOD relationships derived from the V-groove weld model is essentially unchanged with regard to the corresponding fracture resistance data based on the SSR [28] expression. Remarkably, the CTOD $-R$ curves based on $\delta_{ECT}$ and $\delta_{DCG}$ are also fairly indistinguishable from each other. Observe, however, that the latter curves are consistently higher than the corresponding fracture resistance

**Table 2**
Coefficients for the polynomial fitting of $\eta_{J\_CMOD}$-values defined by Eq. (11).

| | Girth Weld Material | $b_0$ | $b_1$ | $b_2$ | $b_3$ |
|---|---|---|---|---|---|
| 2-D | API X80 | 0.950 | 0.622 | −4.099 | 3.548 |
| | UNS N06625 | 0.600 | 3.164 | −9.506 | 7.461 |
| | ASTM A106 | 1.015 | −0.019 | −1.839 | 1.064 |
| 3-D | UNS N06625 | 0.717 | 2.003 | −6.635 | 5.282 |

**Table 3**
Coefficients for the polynomial fitting of $\eta_{J-LLDD}$-values defined by Eq. (12).

| | Girth Weld Material | $c_0$ | $c_1$ | $c_2$ | $c_3$ | $c_4$ | $c_5$ |
|---|---|---|---|---|---|---|---|
| 2-D | API X80 | 1.646 | −10.023 | 57.288 | −141.889 | 153.709 | −60.667 |
| | UNS N06625 | 1.380 | −6.643 | 40.875 | −103.908 | 111.500 | −42.500 |
| | ASTM A106 | −9.281 | 112.627 | −493.106 | 1067.842 | −1141.875 | 479.000 |
| 3-D | UNS N06625 | −1.437 | 25.001 | −100.597 | 205.308 | −218.292 | 95.333 |

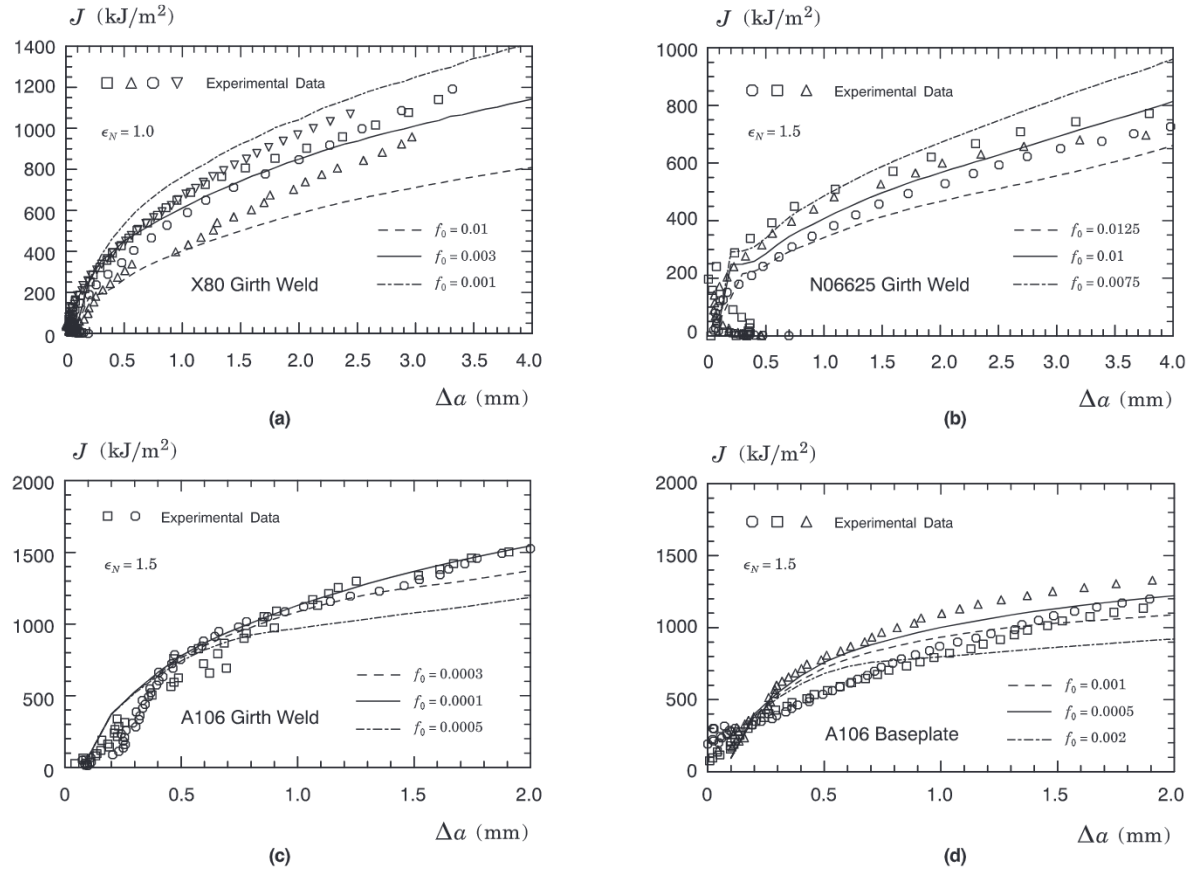


**Fig. 12.** Predicted $J-\Delta a$ curves for the tested girth welds and the baseplate material using the cell size $D/2 = 100$ μm, $f_N = 0.5$ and $s_N = 0.05$ in all computations: (a) API X80. (b) UNS N06625 alloy. (c) ASTM A106 Gr C girth weld. (d) ASTM A106 Gr C baseplate steel.

curves based on $J-$CTOD relationships. Now direct attention to the CTOD $-\Delta a$ data for the A106 girth weld and the baseplate material shown in Fig. 13(c-d). The overall trends remain similar except that the variation of $\delta_{ECT}$ and $\delta_{DCG}$ with crack growth and the fracture resistance data derived from $J-$CTOD relationships differ by a larger amount. Moreover, and perhaps equally importantly, a noteworthy feature of these results is that, in every case considered, the CTOD resistance data based on the double clip gage method to determine $\delta_{DCG}$, is again always higher than the CTOD resistance curves based on $J-$CTOD relationships.

The relatively close correspondence between the variation of $\delta_{ECT}$ and $\delta_{DCG}$ with $\Delta a$ deserves further discussion. As already described in Section 2.2, because $\delta_{DCG}$ is defined as the crack opening at the position of the original crack tip, not the extending crack tip, it should rather be the case that $\delta_{DCG} - \Delta a$ data should in general differ from the corresponding $\delta_{ECT}$ resistance data. However, a different reason is offered here for the weak dependence of CTOD resistance data on the CTOD model, whether using the DCG procedure or the 90° intercept procedure based on the extending crack tip. Fig. 14 shows the deformed profiles for the X80 girth weld test specimen at two different amounts of ductile tearing, as characterized by $\Delta a = 2$ mm and $\Delta a = 4$ mm- observe that the latter level of tearing is slightly larger than the maximum experimental growth given in Fig. 4(a). For both amounts of tearing, there is no sign of significant specimen rotation despite the large imposed remote loading which, in turn, causes the crack to open in a parallel fashion. Because the CTOD for the extending crack is defined here by the intercept between a straight line at 45° from the current crack tip and the deformed crack flanks, it is clear from the plots shown in Fig. 14 that $\delta_{ECT}$ should compare well with $\delta_{DCG}$ in the present framework.

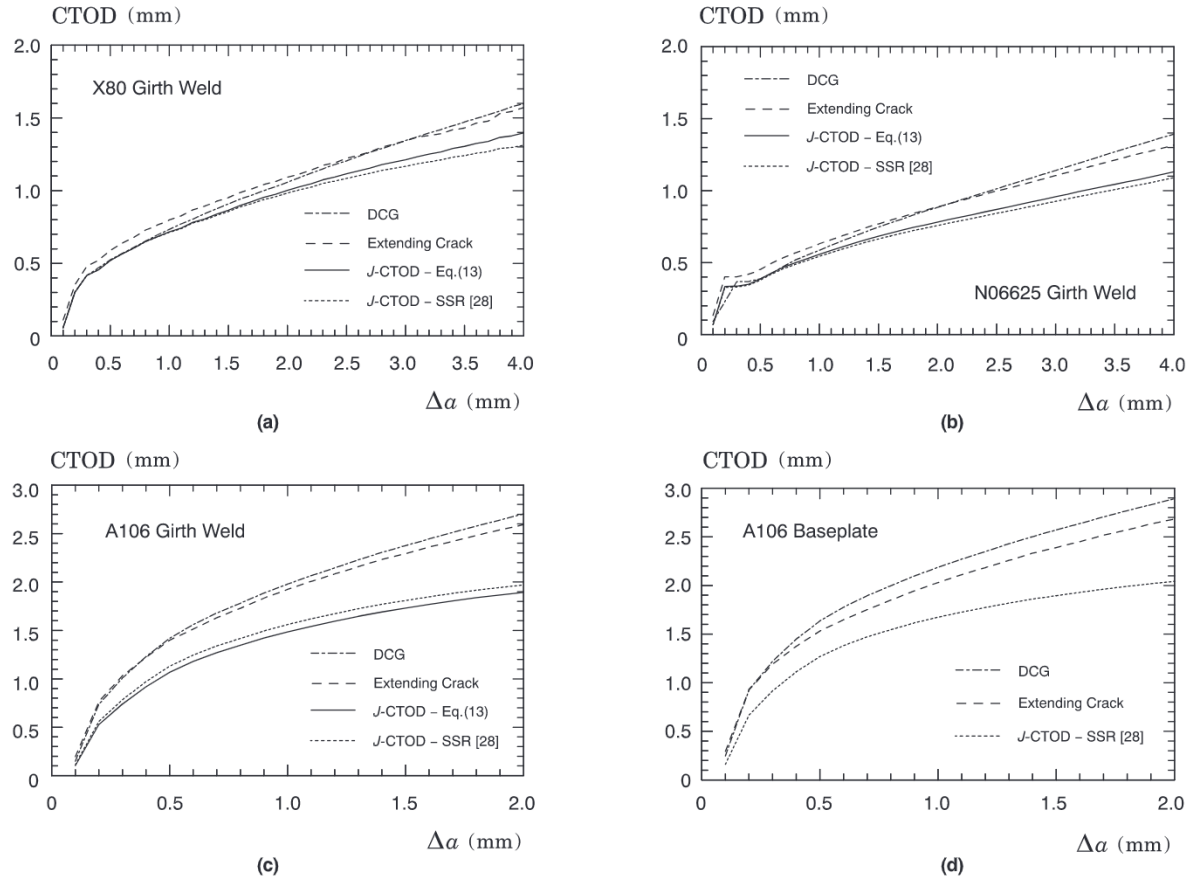


**Fig. 13.** CTOD-resistance curves derived from plane-strain analysis using several procedures: (a) API X80. (b) UNS N06625 alloy. (c) ASTM A106 Gr C girth weld. (d) ASTM A106 Gr C baseplate.

**Table 4**
Coefficients for the polynomial fitting of $m$-values defined by Eq. (13).

| | Girth Weld Material | $d_0$ | $d_1$ | $d_2$ | $d_3$ |
|---|---|---|---|---|---|
| 2-D | API X80 | 1.256 | −0.129 | −0.068 | −0.071 |
| | UNS N06625 | 1.633 | −1.531 | 2.544 | −1.423 |
| | ASTM A106 | 1.581 | −0.626 | 0.424 | −0.119 |
| 3-D | UNS N06625 | 1.565 | −0.731 | 1.541 | −1.344 |

**Table 5**
Calibrated GTN parameters and factors $q_1, q_2$ derived from the work of Faleskog and Shih [48] for all tested materials.

| Tested Material | $e_N$ | $f_0$ | $q_1$ | $q_2$ |
|---|---|---|---|---|
| API X80 weld | 1.0 | 0.0030 | 1.58 | 1.04 |
| UNS N06625 weld | 1.5 | 0.0100 | 1.52 | 0.92 |
| ASTM A106 weld | 1.5 | 0.0001 | 1.75 | 0.80 |
| ASTM A106 steel | 1.5 | 0.0005 | 1.45 | 0.95 |

*5.2.3. CTOD-R curves of the dissimilar Ni-Cr girth weld based on 3-D analyses*

The study thus far has focused on obtaining CTOD resistance data for the tested girth welds by determining CTOD values on the basis of 2-D, plane-strain analyses. Hence, it is natural to raise the question as to whether 3-D effects play a role in changing the ductile fracture response in terms of CTOD −$\Delta a$ data. For the purpose of addressing this issue, this section considers the evaluation of CTOD resistance curves for the dissimilar Ni-Cr girth weld based on $\eta$-factors and $J$ −CTOD relationships derived from 3-D analyses of the V-groove weld model already previously described with the CTOD resistance data based on the DCG method measured by Sarzosa et al. [38].

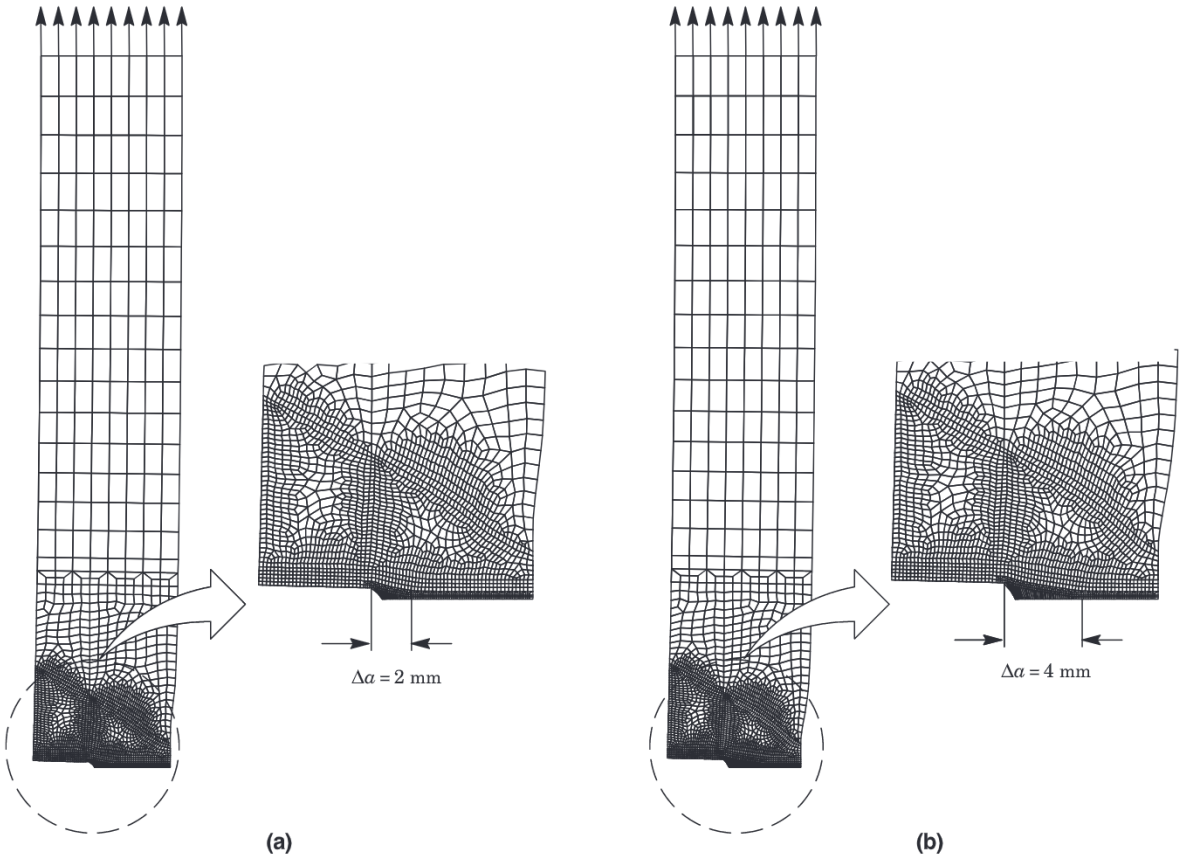


**Fig. 14.** Deformed profiles for the X80 girth weld test specimen at two different amounts of ductile tearing: (a) $\Delta a = 2$ mm. (b) $\Delta a = 4$ mm.

Before undertaking these studies, additional insight can be gained by first examining 3-D effects on the $J$ and CTOD distribution over the crack front for the tested girth welds under consideration. Fig. 15(a-b) display the distribution of $J$ over the crack front, denoted $J_{local}$, with increased levels of loading for the 3-D V-groove weld model with $a/W = 0.3$ and 0.5; this range of $a/W$-ratio represents the amount of ductile tearing ($\tilde{}$4 mm) observed in the fracture tests. The $J_{local}$-values are normalized by the thickness average values, denoted $J_{avg}$, so that the ratio $J_{local}/J_{avg}$ defines the relative change of the local $J$-value with the thickness average value of $J$. Note that the quantity $J_{avg}$ describes the experimental measure of $J$ that would be determined from a $J$-integral fracture test using the plastic work associated with load–displacement records [5,7,23,55]. Fig. 15(c-d) show the corresponding distribution of CTOD, as defined by the 90° intercept procedure, over the crack front, denoted $\delta_{local}$, normalized by the CTOD-value evaluated at the specimen midplane, denoted $\delta_{Z=0}$.

The results shown in Fig. 15(a-b) reveal that, while the maximum $J$-values occur over a relatively small portion of the specimen midplane region ($0 \leqslant Z/(B_N/2) \leq 0.3$) for both $a/W$-ratios, they gradually decrease to smaller $J$-values, which are nevertheless relatively close to the midplane values as the side-groove region is approached. By contrast, the distributions of $\delta_{local}$ across the specimen net thickness shown in Fig. 15(c-d) are uniform over the entire crack front. Further, observe that the $\delta_{local}$-values are virtually indistinguishable from the midplane CTOD value. Such results are consistent with the expected behavior of a tension-loaded specimen, such as the clamped SE(T) geometry analyzed here, indicated in the deformation plots shown in Fig. 14 since the crack faces clearly open rather uniformly over the entire crack front. Moreover, since the CTOD conventionally measured in fracture tests is actually defined by crack tip opening displacement evaluated at the specimen midplane, the results provided in Fig. 15 also indicate a good correlation between the experimentally measured CTOD and thickness average value of $J$.

Now, a similar approach as before may be followed to evaluate the $J$-resistance curves for the UNS N06625 girth weld in which new $\eta$-factors derived from the 3-D analysis of the V-groove weld model are employed to evaluate the $J$-values at each partial unloading point. Tables 2,3 also provide the fitting coefficients derived from the 3-D models that were used in conjunction with Eqs. (11) and (12) to obtain new fracture resistance data for this girth weld. Fig. 16(a) displays the $J$-resistance curves in which the effect of crack growth correction on $J-\Delta a$ data is also examined. These results show that crack growth correction (open symbols) lowers the measured fracture resistance curves by 10–15% for $\Delta a \geqslant 3$ mm compared to the uncorrected data (solid symbols); this finding is fully in accord with previous experimental studies by Mathias et al. [4].

Numerical evaluation of the $J-\Delta a$ response for the 3-D finite element model incorporating crack growth now proceeds by calibrating the set of GTN parameters that establish the best agreement with the $J$-resistance data shown in Fig. 16(a). Because our primary

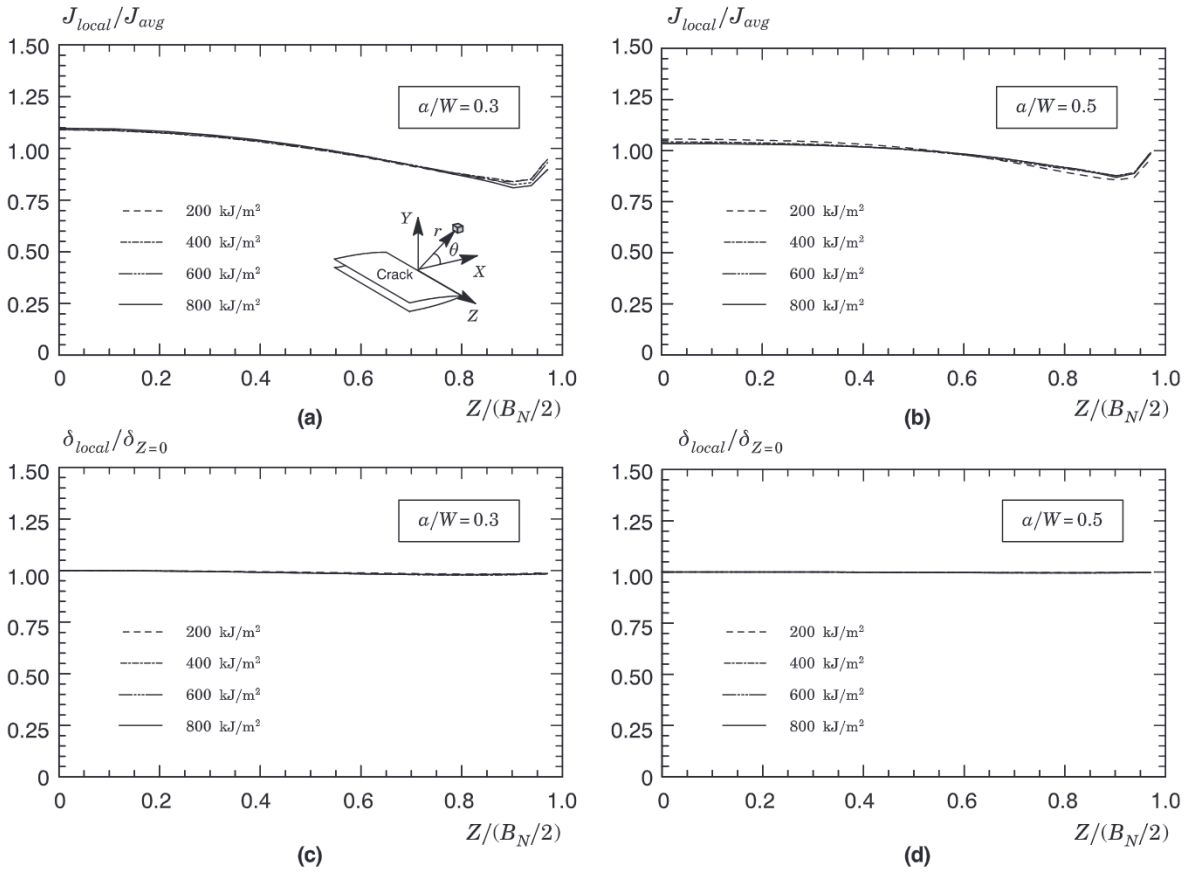


**Fig. 15.** (a) Distribution of $J$ over the crack front, denoted $J_{local}$, with increased levels of loading for the 3-D V-groove weld model with $a/W = 0.3$ and 0.5. (b) Distribution of CTOD, as defined by the 90° intercept procedure, over the crack front, denoted $\delta_{local}$, with increased levels of loading for the 3-D V-groove weld model with $a/W = 0.3$ and 0.5.

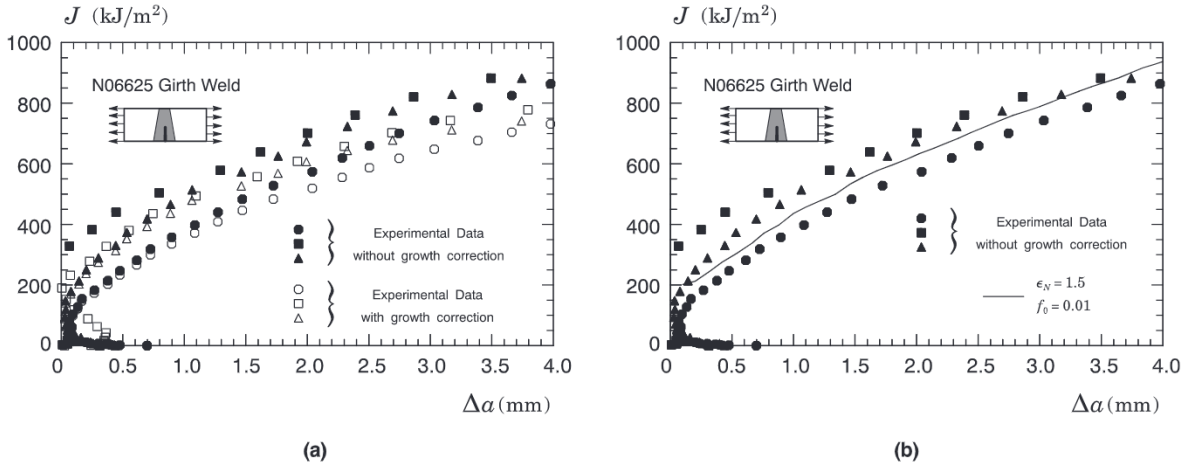


**Fig. 16.** (a) $J$-resistance curves for the UNS N06625 girth weld with new $\eta$-factors derived from the 3-D analysis of the V-groove weld model. (b) Predicted $J-\Delta a$ curve for the uncorrected data (without crack growth correction) using $\epsilon_N = 1.5$ and $f_0 = 0.01$.

interest here lies in the correlation of CTOD $-\Delta a$ data derived from the 3-D numerical analysis with the CTOD resistance curve measured by Sarzosa et al. [38], the calibration procedure focuses on the uncorrected $J$-resistance data (*i.e.*, without crack growth correction).Fig. 16(b) recasts the uncorrected fracture resistance data and includes the predicted resistance curve obtained by using $\epsilon_N = 1.5$ and $f_0 = 0.01$ while keeping other parameters the same as the plane-strain analyses already described. In the context of the

present 3-D analysis, numerical evaluation of ductile crack extension, $\Delta a$, is performed in a similar fashion to the 9-point procedure adopted by current fracture resistance test procedures, including ASTM E1820 [22]. Hence, the amount of crack growth associated with the predicted fracture resistance response represents the *average* crack extension not the midplane growth. Apart from the early stage of ductile crack growth, generally good agreement exists between the measured data and the computed resistance curve.

We will now use the numerical $J$-resistance curve in Fig. 16(b)(b) to determine the corresponding CTOD resistance data including 3-D effects on the fracture response for the tested specimens and how it compares with the experimental CTOD-resistance curves for this N06625 girth weld reported by Sarzosa et al. [38] using the DCG technique. For this purpose, we also consider a new $J-$CTOD relationship, as characterized by parameter $m$, derived from the 3-D analysis of the V-groove weld model given by Eq. (13) with the fitting coefficients also given in Table 4. Fig. 17 compares the CTOD-resistance curve derived from using Eq. (6) with the new $J-$CTOD relationship in 3-D setting and the corresponding CTOD $-\Delta a$ data in which the double clip gage (DCG) method is employed to generate CTOD values for the 3-D numerical model of the V-groove weld. To illustrate the 3-D effects on the computed fracture resistance data, the figure also includes the CTOD resistance curve derived from the DCG procedure based on plane-strain results displayed in previous Fig. 13 - note here that those results are generated from a $J$-resistance curve which incorporates crack growth correction.

The trend displayed by these results is clear as the CTOD $-\Delta a$ data derived from the DCG method lie above the corresponding fracture resistance curve based on the computed $J-$CTOD relationship. Further, the plane-strain DCG results are in relatively close agreement with the present 3-D analysis, a behavior which is consistent with the observed 3-D effects on the $J$ and CTOD distribution over the crack front shown in Fig. 15. The tendency for the CTOD resistance curve based on the DCG procedure to lie always above the CTOD $-\Delta a$ data derived from the $J-$CTOD relationship has also been noted in previous efforts to investigate fracture resistance behavior in terms of CTOD by Sarzosa et al. [38] and Weeks and Lucon [19]. At the same time, it is clear from the figure that the computed CTOD resistance curve based on the DCG method agrees relatively well with the measured data, albeit lying somewhat below the experimental resistance curve. While we have not explored the source of the small deviation between both CTOD resistance curves based on the DCG method, these results suggest a potential effect of key test parameters on the measured data. For example, the 3-D numerical model has a straight, through crack whereas the crack front of the tested fracture specimen not only exhibits a certain degree of curvature but the crack front is also rather nonuniform [56]. Aside from these uncertainties, the double clip gage method no doubt produces higher CTOD resistance curves compared with the corresponding fracture resistance data based on $J-$CTOD relationships which, thus, gives nonconservative estimates of fracture toughness.

## 6. Summary and conclusions

This study describes a numerical investigation of stable ductile extension in pipe girth welds with different material properties to characterize the crack growth resistance behavior in terms of the $J$-integral and crack tip opening displacement (CTOD). The procedure laid out for describing the evolution of $J$ and CTOD with increased loading for an extending crack involves applying a computational cell methodology to model Mode I crack extension in plane strain and 3-D models for clamped SE(T) specimens with a weld centerline crack. The investigation also covers fracture resistance tests of pipe girth welds with different levels of weld strength mismatch, including a dissimilar welded specimen extracted from a clad line pipe, from which key microstructural parameters utilized in the growth analysis are calibrated. The extensive numerical analyses are employed to determine CTOD fracture resistance curves on the basis of the following approaches: (1) CTOD-values converted from corresponding $J$-values of the fracture resistance data; (2) CTOD-values evaluated using the 90° intercept procedure based on the *extending* crack tip and the deformed crack flanks and (3) CTOD-values based on the double clip gage (DCG) procedure. Predictions from the numerical analyses are also compared with experimentally measured CTOD resistance data based on the DCG method.

The present investigation shows that the evaluation procedure of $J$-resistance curves based on plastic work is not significantly affected by the degrees of weld strength mismatch considered in the study. Our analyses reveal that factors $\eta_{J-CMOD}$ derived from plane-

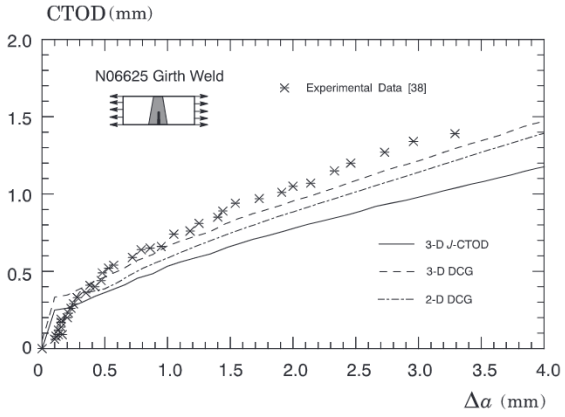


**Fig. 17.** Comparison of CTOD resistance curves derived from the double clip gage method and $J-$CTOD relationship for the 3-D V-groove weld model of the UNS N06625 girth weld.

strain models of clamped SE(T) geometries with V-groove welds compare well with corresponding $\eta$-values applicable to homogeneous materials, particularly in the range $a/W \leq 0.2$–0.45. By contrast, factors $\eta_{J-LLD}$ show a more noticeable dependence on weld strength mismatch. Overall, however, since $\eta_{J-LLD}$ only enters into the evaluation procedure to correct $J$ for crack growth, this effect may be expected to be relatively small. Similarly, the $J$ –CTOD relationships are only weakly sensitive to the degree of weld strength mismatch.

The extensive set of growth analyses performed on clamped SE(T) specimens with weld centerline cracks and varying levels of weld strength mismatch reveals important differences between CTOD values based on the double clip gage (DCG) method and the $\delta$-values derived from $J$ –CTOD relationships. Indeed, in every case considered in this study, including detailed 3-D analysis of a fracture specimen extracted from a dissimilar Ni-Cr girth weld, the CTOD resistance curve based on the DCG approach was always consistently higher than the corresponding CTOD resistance data directly obtained from a $J$-resistance curve. Such differences are of particular concern in defect assessment procedures and ECA methodologies since the DCG method clearly provides nonconservative estimates of fracture toughness. A possible alternative to circumvent this issue would be to determine the crack driving force in the cracked component also using the DCG method so that the measured fracture toughness value and the crack tip loading parameter would be both consistent. However, this approach would also involve more computational effort and, thus, would not always be easily obtained for engineering applications and routine FFS analyses.

## Declaration of Competing Interest

The authors declare that they have no known competing financial interests or personal relationships that could have appeared to influence the work reported in this paper.

## Acknowledgments

This investigation is supported by the Brazilian Council for Scientific and Technological Development (CNPq) through Grant 302853/2018-9. The authors acknowledge Petrobras for providing additional support for the work described here and for making available the experimental data. The authors are also indebted to Professor Diego F. B. Sarzosa (University of São Paulo) for his assistance in fracture testing and for the helpful discussions.

## References

[1] Rice JR. A path independent integral and the approximate analysis of strain concentration by notches and cracks. J Appl Mech 1968;35:379–86.
[2] Hutchinson JW. Fundamentals of the phenomenological theory of nonlinear fracture mechanics. J Appl Mech 1983;50:1042–51.
[3] Joyce JA, Hackett EM, Roe C. Effects of crack depth and mode loading on the J-R curve behavior of a high strength steel. In: Underwood JH, Schwalbe K-H, Dodds RH, editors. Constraint effects in fracture, ASTM STP 1171. Philadelphia: American Society for Testing and Materials; 1993. p. 239–63.
[4] Mathias LLS, Sarzosa DFB, Ruggieri C. Effects of specimen geometry and loading mode on crack growth resistance curves of a high-strength pipeline girth weld. Int J Press Vessels Pip 2013;111–112:106–19.
[5] Anderson TL. Fracture mechanics: fundaments and applications. 3rd ed. Boca Raton, FL: CRC Press; 2005.
[6] Nyhus B, Polanco M, Ørjasæter O. SENT specimens as an alternative to SENB specimens for fracture mechanics testing of pipelines. In: 22nd International conference on Ocean, Offshore and Arctic Engineering (OMAE), Vancouver, Canada; 2003.
[7] Cravero S, Ruggieri C. Estimation procedure of J-resistance curves for SE(T) fracture specimens using unloading compliance. Eng Fract Mech 2007;74:2735–57.
[8] Clarke GA, Andrews WR, Paris PC, Schmidt DW. Single specimen tests for J_Ic determination. In: Rice JR, Paris PC, editors. Mechanics of crack growth, ASTM STP 590. Philadelphia: American Society for Testing and Materials; 1976. p. 27–42.
[9] Landes JD, Begley JA. Recent developments in J_Ic testing. In: Brown WF, Kaufman JG, editors. Developments in fracture mechanics test methods standardization, ASTM STP 632. Philadelphia: American Society for Testing and Materials; 1977. p. 57–82.
[10] Ruggieri C. Further results in J and CTOD estimation procedures for SE(T) fracture specimens – Part I: Homogeneous materials. Eng Fract Mech 2012;79:245–65.
[11] Paredes M, Ruggieri C. Further results in J and CTOD estimation procedures for SE(T) fracture specimens – Part II: weld centerline cracks. Eng Fract Mech 2012;89:24–39.
[12] Zhu XK, McGaughy T. A review of fracture toughness testing and evaluation using sent specimens. In: 10th International Pipeline Conference (IPC), Calgary, Canada; 2014.
[13] Ruggieri C. Low constraint fracture toughness testing using se(t) and se(b) specimens. Int J Press Vessels Pip 2017;156:23–39.
[14] Zhu XK. Review of fracture toughness test methods for ductile materials in low-constraint conditions. Int J Pressure Vessel Pip 2016;139–140:173–83.
[15] Burdekin FM, Stone DEW. The crack opening displacement approach to fracture mechanics in yielding materials. J Strain Anal 1966;1:145–53.
[16] Harrison JD, Dawes MG, Archer GL, Kamath MS. The COD approach and its application to welded structures. In: Landes JD, Begley JA, Clarke GA, editors. Elastic-plastic fracture, ASTM STP 668. Philadelphia: American Society for Testing and Materials; 1979. p. 606–31.
[17] Moore PL, Pisarski HG. Validation of methods to determine CTOD from SENT specimens. In: 22nd International Offshore and Polar Engineering Conference (ISOPE), Rhodes, Greece; 2012.
[18] ExxonMobil Upstream, Measurements of crack-tip opening displacement (CTOD) fracture resistance curves using single-edge notched tension (SENT) specimens, Tech. rep.; 2010.
[19] Weeks TS, Lucon E. Direct comparison of single-specimen clamped SE(T) test methods on X100 line pipe steel. In: 10th International Pipeline Conference (IPC), Calgary, Canada; 2014.
[20] British Institution, Method of test for determination of fracture toughness in metallic materials using single edge notched tension (SENT) specimens, BS 8571; 2018.
[21] Zhu XK, Joyce JA. Review of fracture toughness (G, K, J, CTOD, CTOA) testing and standardization. Eng Fract Mech 2012;86:1–46.
[22] American Society for Testing and Materials, Standard test method for measurement of fracture toughness, ASTM E1820-17; 2017.
[23] Cravero S, Ruggieri C. Further developments in J evaluation procedure for growing cracks based on LLD and CMOD data. Int J Fract 2007;148:387–400.
[24] Zhu X-K. Progress in development of fracture toughness test methods for SENT specimens. Int J Press Vessels Pip 2017;156:40–58.
[25] Park DY, Tyson WR, Gravel JP. CANMET SENT test method, updates and applications. Int J Press Vessels Pip 2017;156:8–16.
[26] Shih CF. Relationship between the J-integral and the crack opening displacement for stationary and extending cracks. J Mech Phys Solids 1981;29:305–26.

[27] International Organization for Standardization, Metallic materials – method of test for the determination of quasistatic fracture toughness of welds, ISO 15653-2010; 2010.
[28] Sarzosa DFB, Souza RF, Ruggieri C. J-CTOD relations in clamped SE(T) fracture specimens including 3-D stationary and growth analysis. Eng Fract Mech 2015;147:331–54.
[29] Shih CF, deLorenzi HG, Andrews WR. Studies on crack initiation and stable crack growth. In: Landes JD, Begley JA, Clarke GA, editors. Elastic-plastic fracture, ASTM STP 668. Philadelphia: American Society for Testing and Materials; 1979. p. 65–120.
[30] American Petroleum Institute. Specification for line pipe. API 2007;5L.
[31] American Society for Testing and Materials, Standard specification for Nickel-Chromium-Molybdenum-Columbium alloy (UNS N06625) and Nickel-Chromium-Molybdenum-Silicon alloy (UNS N06219) plate, sheet, and strip, ASTM B443-00; 2009.
[32] American Society for Testing and Materials, Standard specification for Nickel-Chromium-Molybdenum-Columbium alloys (UNS N06625 and UNS N06852) and Nickel-Chromium-Molybdenum-Silicon Alloy (UNS N06219) pipe and tube, ASTM B444-06 (2011).
[33] American Society for Testing and Materials, Standard specification for seamless carbon steel pipe for high-temperature service, ASTM A106; 2015.
[34] American Petroleum Institute, Fitness-for-service, API RP-579-1/ ASME FFS-1; 2016.
[35] Ramberg W, Osgood WR. Description of stress-strain curves by three-parameters, Technical Report NACA-TN-902, National Advisory Committee for Aeronautics; 1943.
[36] Ruggieri C. Test procedure for fracture resistance characterization of pipeline steels and pipeline girth welds using single-edgenotched tension (SENT) specimens, Tech. rep., University of Sao Paulo; 2020.
[37] Souza RF, Ruggieri C. Revised wide range compliance solutions for selected standard and non-standard fracture test specimens based on crack mouth opening displacement. Eng Fract Mech 2017;178:77–92.
[38] Sarzosa DFB, Barbosa VS, Santos CP, Hippert E, Ruggieri C. Fracture resistance testing of dissimilar nickel-chromium girth welds for clad line pipes. Int J Fract 2017;205(2):168–88.
[39] Joyce JA. Manual on elastic-plastic fracture: Laboratory test procedure, ASTM Manual Series MNL 27, ASTM International; 1996.
[40] Joyce JA, Link RE. Effects of constraint on upper shelf fracture toughness. In: Reuter WG, Underwood JH, Newman J, editors. Fracture mechanics, ASTM STP 1256. Philadelphia: American Society for Testing and Materials; 1995. p. 142–77.
[41] Ferreira C, Sarzosa DFB, Ruggieri C. Fracture toughness testing of an overmatched pipe girth weld using clamped SE(T) specimens. In: ASME 2019 Pressure Vessels & Piping Conference (PVP 2019), San Antonio, TX; 2019.
[42] Xia L, Shih CF. Ductile crack growth – I: A numerical study using computational cells with microstructurally-based length scales. J Mech Phys Solids 1995;43:223–59.
[43] Ruggieri C, Dodds RH. Numerical modeling of ductile crack growth using computational cell elements. Int J Fract 1996;82:67–95.
[44] Gullerud AS, Gao X, Dodds RH, Haj-Ali R. Simulation of ductile crack growth using computational cells: numerical aspects. Eng Fract Mech 2000;66:65–92.
[45] Garrison Jr WM, Moody NR. Ductile fracture. J Phys Chem Solids 1987;48:1035–74.
[46] Gurson AL. Continuum theory of ductile rupture by void nucleation and growth: Part I – Yield criteria and flow rules for porous ductile media. J Eng Mater Technol 1977;99:2–15.
[47] Tvergaard V. Material failure by void growth to coalescence. Adv Appl Mech 1990;27:83–151.
[48] Faleskog J, Shih C. Cell model for nonlinear fracture analysis – I: Micromechanics calibration. Int J Fract 1998;89:355–73.
[49] Chu CC, Needleman A. Void nucleation effects in biaxially stretched sheets. J Eng Mater Technol 1980;102:249–56.
[50] Besson J. Continuum models of ductile fracture: a review. Int J Damage Mech 2010;10:3–52.
[51] Healy B, Gullerud A, Koppenhoefer K, Roy A, RoyChowdhury S, Petti J, et al. WARP3D: 3-D nonlinear finite element analysis of solids for fracture and fatigue processes, Tech. rep., University of Illinois at Urbana-Champaign; 2014, http://code.google.com/p/warp3d.
[52] Ruggieri C. FRACTUS2D: Numerical computation of fracture mechanics parameters for 2-D cracked solids, Tech. rep., University of Sao Paulo; 2011.
[53] Moran B, Shih CF. A general treatment of crack tip contour integrals. Int J Fract 1987;35:295–310.
[54] Ruggieri C, Dotta F. Numerical modeling of ductile crack extension in high pressure pipelines with longitudinal flaws. Eng Struct 2011;33:1423–38.
[55] Kanninen MF, Popelar CH. Advanced fracture mechanics. New York: Oxford University Press; 1985.
[56] Sarzosa DFB. Personal communication; 2020.